**Theses and Dissertations**

Summer 2012

# Design and application of an instrumented pendulum device for measuring energy absorption during fracture insult in large animal joints in vivo

Bryce Diestelmeier
*University of Iowa*

DESIGN AND APPLICATION OF AN INSTRUMENTED PENDULUM DEVICE

FOR MEASURING ENERGY ABSORPTION DURING FRACTURE INSULT IN

LARGE ANIMAL JOINTS *IN VIVO*

by

Bryce Diestelmeier

A thesis submitted in partial fulfillment
of the requirements for the Master of
Science degree in Biomedical Engineering
in the Graduate College of
The University of Iowa

July 2012

Thesis Supervisor:  Professor Thomas D. Brown

Graduate College
The University of Iowa
Iowa City, Iowa

CERTIFICATE OF APPROVAL

_____

MASTER'S THESIS

_____

This is to certify that the Master's thesis of

Bryce Diestelmeier

has been approved by the Examining Committee
for the thesis requirement for the Master of Science
degree in Biomedical Engineering at the July 2012 graduation.

Thesis Committee: _____
                  Thomas D. Brown, Thesis Supervisor


                  _____
                  Yuki Tochigi


                  _____
                  Nicole M. Grosland

ACKNOWLEDGMENTS

TABLE OF CONTENTS

LIST OF TABLES

# LIST OF FIGURES

Figure

viii

LIST OF EQUATIONS

Equation

CHAPTER 1: INTRODUCTION

Osteoarthritis (OA), often referred to as the wear-and-tear arthritis, is the most common joint disease [1]. Its symptoms include joint pain, stiffness, and limited range of motion, which all lead to a lower quality of life [1-5]. Osteoarthritis can be divided into primary and secondary types. Primary OA is an idiopathic phenomenon, while secondary OA is caused by a number of risk factors including injury, obesity, inactivity, and genetics [1-6].

Posttraumatic OA is a subset of secondary OA that develops after distinct synovial joint injury. Synovial joint injuries such as meniscus tears, ligament tears, capsule tears, joint dislocation, chondral injuries, and intraarticular fractures (IAFs) are usually consequences from vehicle accidents, sports, falling, military injuries, or other physical trauma sources [6-11]. To list a few examples of prevalence: lower-extremity injuries from vehicle accidents are the main cause of automobile-related disabilities, approximately 60%-90% of ruptured anterior cruciate ligaments result in posttraumatic OA within 15 years, and over 12% of war-related trauma involves lower-extremity injuries [12-15].

In addition to physical injury and joint degeneration, posttraumatic OA also has significant financial burden [16-24]. It has been recently shown that $12 billion (12%) of the overall annual cost of arthritis treatment in the United States is attributed to lower-extremity posttraumatic OA (Figure 1). Approximately $3.06 billion (26%) of the annual lower-extremity posttraumatic OA costs come directly from U.S. health care expenses. This corresponds to 5.6 million Americans with posttraumatic OA symptoms that are severe enough to require medical attention [7]. Furthermore, patients with posttraumatic OA are frequently younger individuals who are in their prime income earning years [25-27].

**The Cost of Treatment of Arthritis in the
United States in Billions of Dollars**

11.8    16.5

86.1

RA
OA
Posttraumatic OA
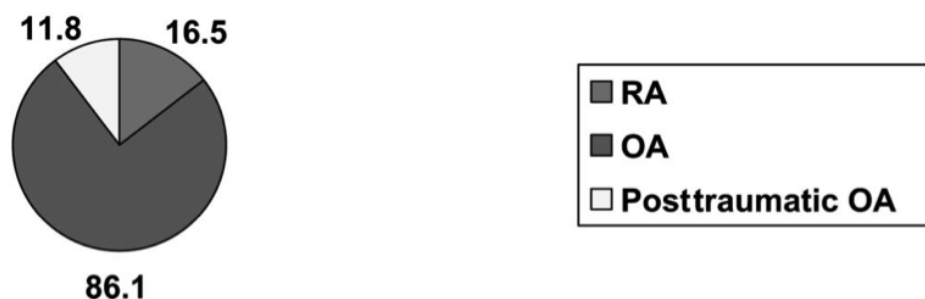
Figure 1.    The cost of treatment of arthritis in the United States per year is $114.5 billion, and the distribution between rheumatoid arthritis (RA), non-posttraumatic OA, and posttraumatic OA is demonstrated. Image adapted and reproduced from Brown et al. [7].

It is evident that posttraumatic OA is of significant importance to society physically and financially. Consequently, posttraumatic OA has been drawing increasing attention. Despite progress in this research field during the last couple of decades, however, the mechanisms leading to posttraumatic OA are still not fully understood. Additionally, advancements in surgical treatment techniques have progressed, but the risk of posttraumatic OA has still remained unacceptably high (Figure 2) [28]. In fact, over half of patients with tibial plafond fractures develop posttraumatic OA within two years, even with conventional treatment strategies [29-31].

In order to progress in this field, it is first necessary to create appropriate survival animal models in which posttraumatic OA predictably develops in a manner consistent with that in clinical settings. Once these models have been developed, they will enable effective preclinical trials of prevention and treatment therapies. Such models need to reproducibly replicate the pathophysiology involved in posttraumatic OA. There are several well-recognized factors that contribute much to the pathogenesis of posttraumatic OA [25, 32-35]. Acute factors include mechanical cartilage injury that involves physical

damage of collagen network and cartilage matrix, accompanied by chondrocyte death that causes dysfunction of cartilage metabolism. Sub-acute factors include biological stimuli leaked from damaged tissue, and those released associated with inflammatory reactions. Chronic factors include cumulative abnormal mechanical stresses to damaged cartilage. These factors are thought to contribute both individually and synergistically to the development of cartilage degeneration.
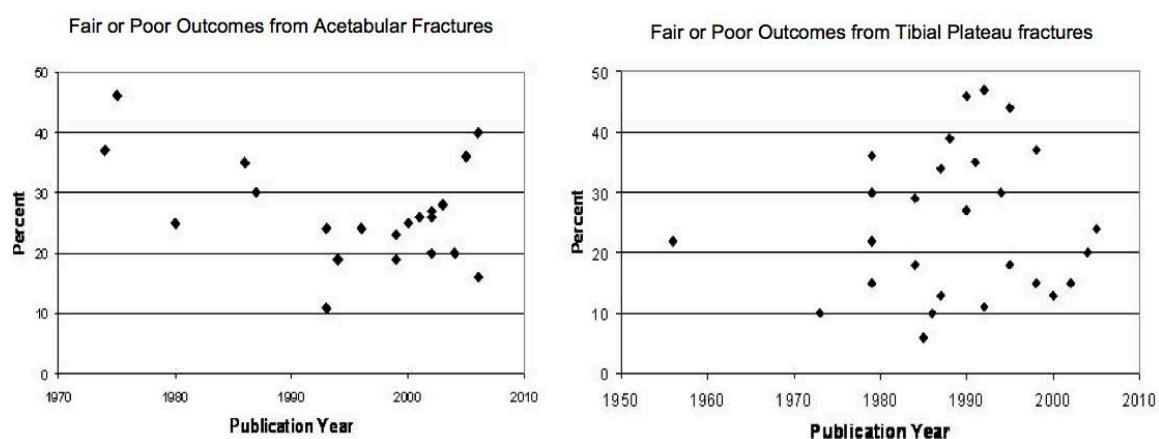


Figure 2:   Percentages of fair and poor outcomes of acetabular and tibial plateau intraarticular fracture treatments. Images adapted and reproduced from McKinley et al. [28].

Of these major factors, acute cartilage injury has been modeled by means of blunt impaction [15, 36-45]. Unfortunately, previous survival animal models using this insult modality did not predictably develop distinct cartilage degeneration in a short- to mid-term [15, 37-39, 41, 42], presumably due to relatively mild cartilage damage, and/or due to a lack of the chronic mechanical factor. Recently, Furman et al. [25] developed a technique to model IAF in the mouse knee *in vivo,* and the insulted joints developed massive cartilage degeneration over a period of 8 weeks. This is a very significant experimental advance, although in its present embodiment it appears limited to relatively

severe fractures, and it exhibits substantial and uncontrolled variability in the location of the fracture lines.

Regardless of insult modality, controllability and reproducibility of achievable injury are crucial for this type of animal model to be effective. Unless consistency of injury severity across experimental groups is ensured, preclinical trials of new treatment cannot be scientifically valid. For this reason, use of an instrumented device capable of measuring the properties of mechanical insult for each individual animal is highly desirable.

<u>1.1 Objective</u>

Development of a large animal survival model of human IAF has been a long-standing work in The University of Iowa Orthopaedic Biomechanics Laboratory. An impaction insult technique to create IAFs in porcine hocks *in vivo*, with the injury mechanisms consistent with those in human clinical injuries, had been developed. A pendulum device that enabled implementing the fracture insult in survival surgery settings also had been designed and built. As noted above, the next logical step was to establish a technique to measure the properties of impaction insult that was executed to create fracture in each individual animal. The purpose of the present work was to design, construct, and evaluate a system to measure the energy absorbed during impaction fracture insult.

In order to guide the initial direction of the proposed model, it was important to investigate other blunt impaction and IAF models that have been developed. Out of these many models, this work will discuss the blunt impaction models developed by Borrelli et al. [36] and Tochigi et al. [46] and the IAF models developed by Furman et al. [25] and Backus et al. [47]. These models were chosen because they have been prominent in posttraumatic OA research, and because they incorporate a broad spectrum of ideas and techniques that are commonly used among other blunt impaction and IAF models.

## 1.2 Blunt Impaction Models

### 1.2.1 Borrelli et al. Pendulum Device

Borrelli et al. [36] designed a pendulum device that delivered energy to the femoral condyle in a rabbit model (Figure 3). The pendulum arm was 0.91 meters in length and its mass was 587 grams. Additional mass could also be added to the pendulum if desired. An electromagnet allowed the pendulum arm to be held at a desired height, and released when necessary. When released, the pendulum arm impacted a padded low-friction trolley equipped with a rigidly fixed impaction platen that transmitted a compressive force pulse to the rabbit femoral condyle that was positioned using an X-Y table. The platen was equipped with a load cell that collected force data at 2 kilohertz using LabVIEW software.

With the dimensions and instrumentation described, it was possible to conveniently acquire (i) the pendulum's initial gravitational potential energy before release, and (ii) the force history of impact. The initial gravitational potential energy, which indicated the magnitude of energy input, was calculated with Equation 1 (below). From the force history data, the maximum force and time to peak force could be acquired as well. This is not unusual for devices equipped solely with load cells for instrumentation [15, 40-44].

In a pilot study using cadaver specimens [36], pressure sensitive film was placed between the impactor and the femoral condyle to measure contact area and contact stress. These additional measurements were not applied to impaction insult *in vivo*, due to difficulty in use of the pressure sensitive film in sterile surgical settings.
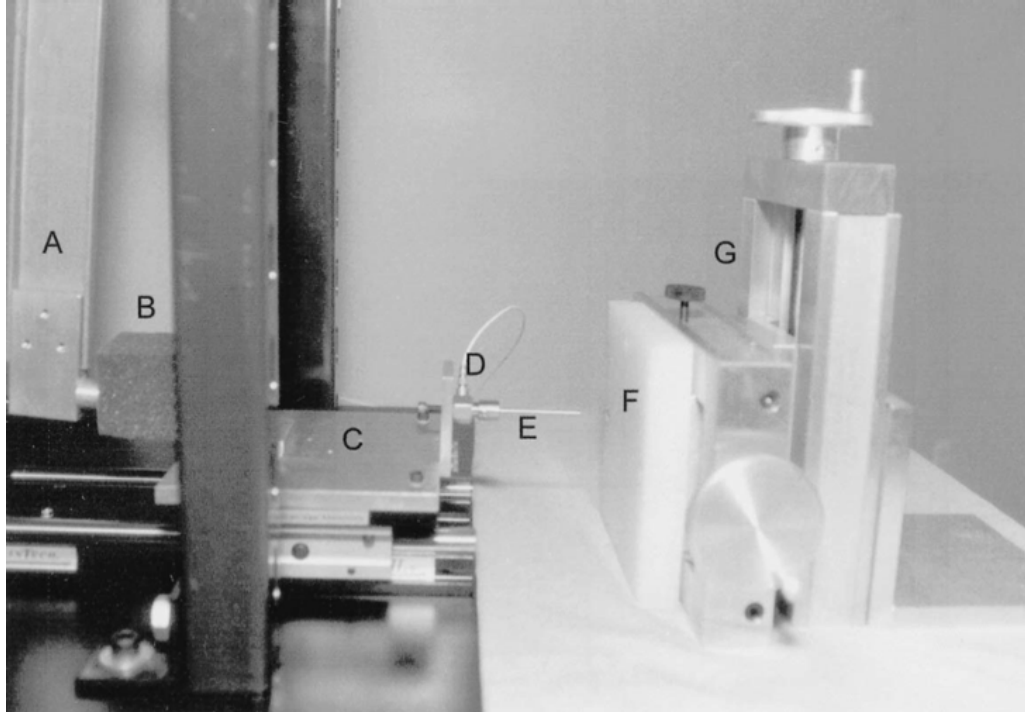
Figure 3:   Close-up view of the components of the Borrelli et al. pendulum device. Pendulum arm (A), foam (B), trolley assembly (C), load cell (D), impactor (E), polyethylene block (F), and X-Y table (G). Image adapted and reproduced from Borrelli et al. [36].

Equation 1:   Equation and variables needed to calculate the initial gravitational potential energy of an impact mass.

### Equation

$$PE = mgh$$

### Variables

$PE$ = potential energy of the pendulum drop mass (in joules)
$m$ = pendulum drop mass (in kilograms)
$g$ = acceleration due to gravity (in meters per second squared)
$h$ = drop height of the pendulum drop mass (in meters)

### 1.2.2 Tochigi et al. Drop Tower

Tochigi et al. [46] designed a drop tower device that delivers energy to the femoral condyle in a rabbit model (Figure 4). The drop tower had a sliding drop mass (1.55 kilograms) that could slide a maximum of 0.45 meters. Rather than attaching additional mass like the Borrelli device, impaction magnitude could easily be controlled by adjusting the drop height. A clamping release mechanism allowed the drop mass to be held at a desired height and released when necessary. When released, the drop mass impacted a platen that would then effectively impact the rabbit femoral condyle that was positioned using a specimen fixation table. The drop mass was equipped with an accelerometer. Acceleration data were collected at 15 kilohertz using LabVIEW software.
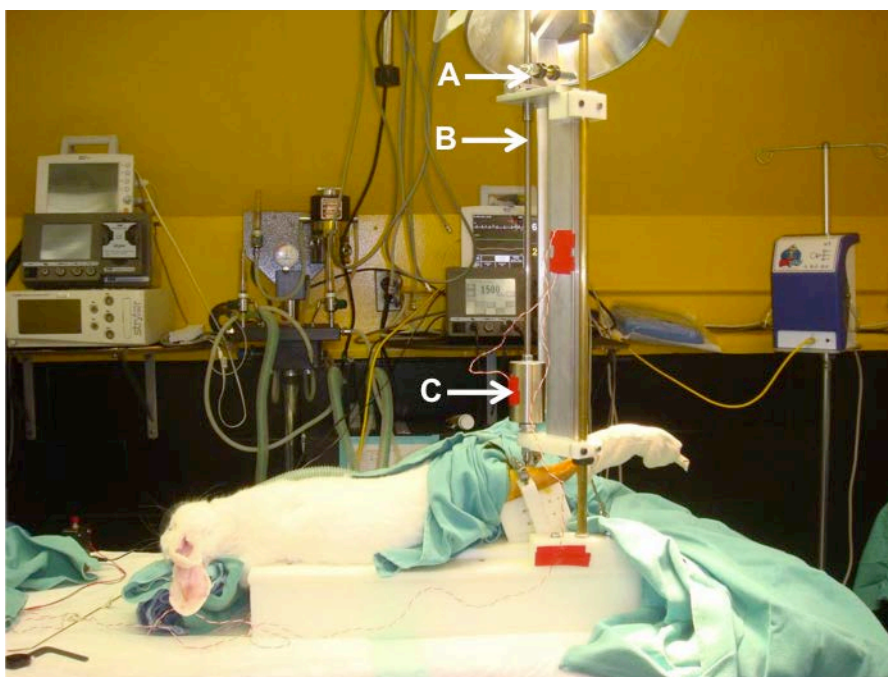


Figure 4:   Tochigi et al. drop tower device in the surgical environment. The clamping release mechanism (A), the drop arm (B), and drop mass with accelerometer inside (C) are labeled.

With the dimensions and instrumentation described, it was possible to conveniently acquire the drop mass's pre-release potential energy (energy input) and the acceleration history of impact. From the acceleration history data, the maximum acceleration and time-to-peak acceleration could be ascertained as well. With the drop mass being known, the acceleration data could be converted to force data.

Patterning after Borrelli's work, a cadaver specimen impaction experiment using pressure sensitive film was conducted to determine the contact area and contact stress of achievable impaction. Again, these additional measurements were not applied to impaction insult *in vivo*.

### 1.3 Intraarticular Fracture Models

#### 1.3.1 Furman et al. Intraarticular Fracture Model

Furman et al. [25] designed a device that delivered energy to the tibial plateau in a mouse model (Figure 5). The device utilized a materials testing system so that the user could control the loading forces, rates of loading, and displacements of impaction. Rigidly fixed to the materials testing system was a wedged-tip indenter that would deliver a focalized compressive force pulse to the tibial plateau. The loading force and rate of loading were 55 newtons and 20 newtons per second, respectively.

From the materials testing system, the force-displacement information could be collected, and the corresponding energy of fracture could be calculated. When compared to the devices with load cells and accelerometers, this technique clearly provides more information. However, it is difficult to mimic a clinically-relevant impaction fracture insult using a materials testing system, because trying to consistently control the high load forces and rates of loading proves to be problematic. Evidence of this is present in the results described by Furman et al. [25]. The energies of fracture that were recorded exhibited a questionably large magnitude and range (33-231 joules). The quantity of the

data that is produced using a materials testing system is appealing, but the issue of

inconsistency can be difficult to overcome.
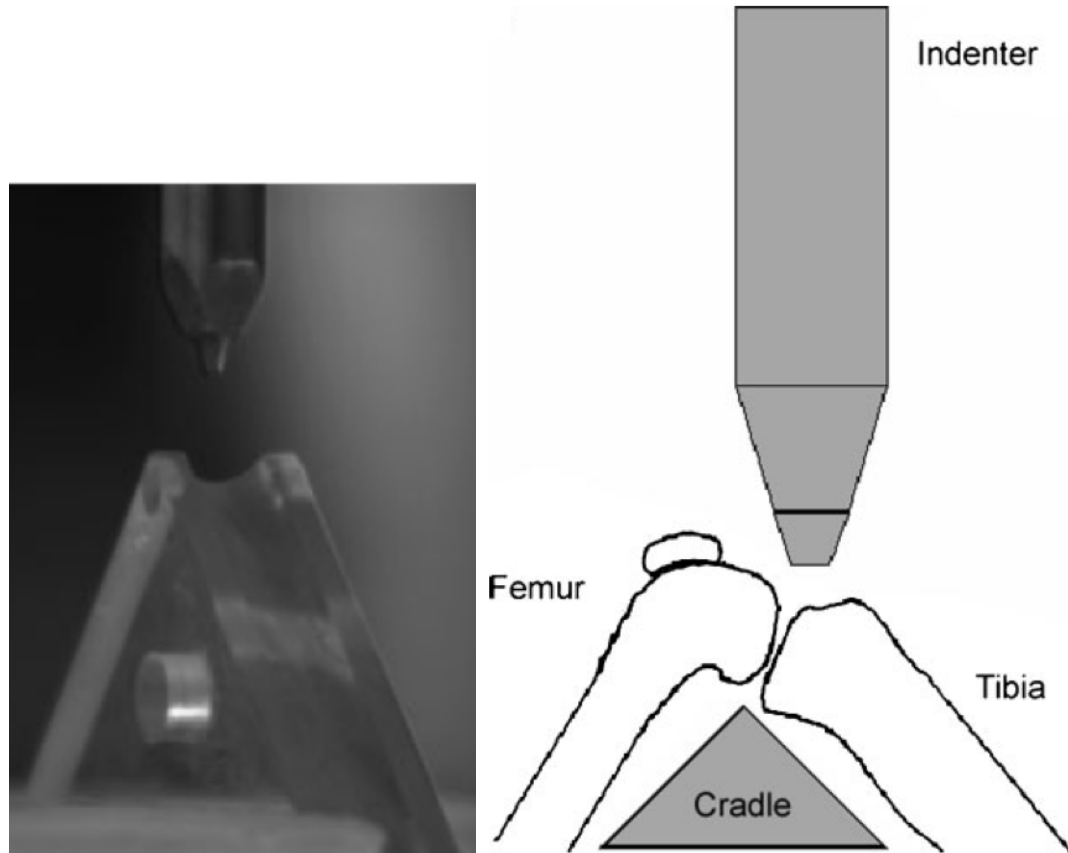


Figure 5:  Cradle and indenter for creating an IAF in the mouse knee. Indenter and
custom lower limb cradle for creating tibial articular fractures (left).
Schematic showing alignment of indenter with tibia during loading (right).
Image adapted and reproduced from Furman et al. [25].

### 1.3.2 Backus et al. Drop Tower Device

Backus et al. [47] designed a drop tower device to model IAF in the porcine knee,

by delivering a high-energy compressive force pulse across the joint (Figure 6). The drop

tower had a sliding drop mass (30 kilograms) that was released from a height of one

meter. When released, the drop mass impacted an aluminum specimen fixture, in which a

cadaver porcine knee (the whole-joint construct) was confined by holding the specimen's tibia and femur in place by using fiberglass reinforced resin and PMMA. The specimen was preloaded (155 kilograms) using six parallel springs that were fixed to opposite ends of the specimen fixture. Below the specimen fixture was a rigidly fixed load cell that could record force history data.

With the dimensions and instrumentation described, it was possible to conveniently acquire the drop mass's pre-release potential energy (energy input) and the force history of impact. It is important to note that, differently from the above-noted systems, this impaction system was designed purely for fracture insult *ex vitro*, because the potting and specimen fixture technique could not be used for *in vivo* scenarios.
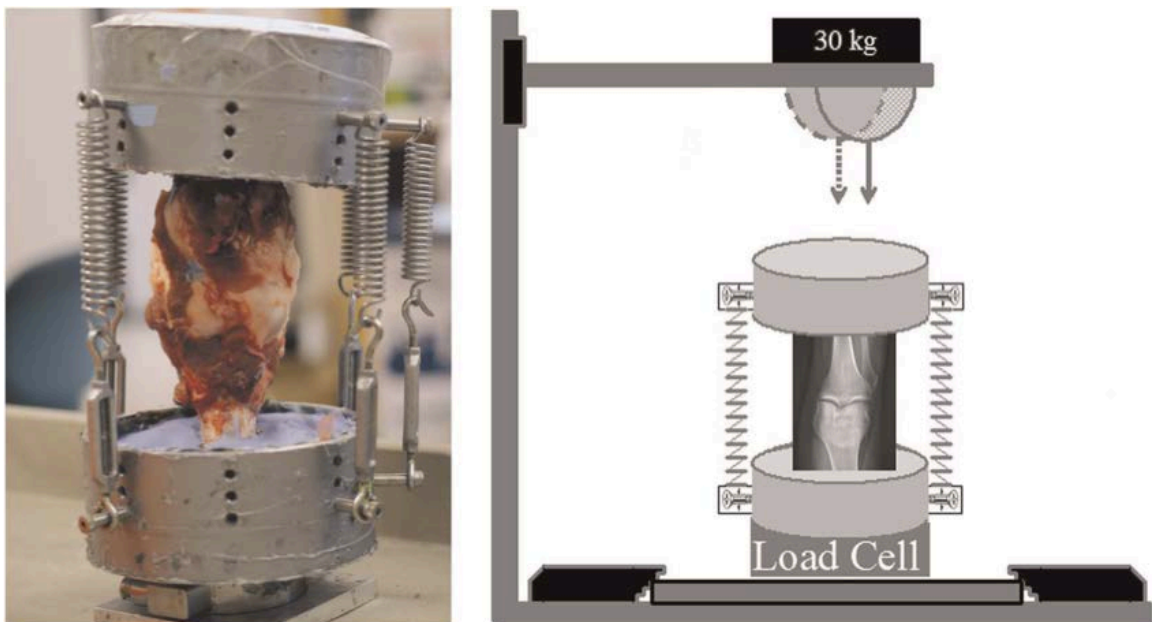


Figure 6:  Preload and impact alignment of closed porcine knee model. Posterior view of knee potted in aluminum fixtures and held with six springs (left). Dashed arrow represents indenter alignment to impact a knee without fracture; solid arrow represents the alignment to impact a knee resulting in an intraarticular fracture (right). Image adapted and reproduced from Backus et al. [47].

## 1.4 Limitations of Previous Models

Previous blunt impaction and IAF models have been fairly successful with inducing posttraumatic OA, but there are still certain limitations that need to be addressed before progressing further in model development. Some of the limitations were alluded to in the previous section, but they will also be reaffirmed here. Models instrumented solely with load cells are only able to collect force history information. Models instrumented solely with accelerometers are only able to collect acceleration history information. With a known drop mass, the acceleration history can be easily used to find force history information. Therefore, models with load cells or accelerometers are limited to force history data. The initial gravitational potential energy of impaction can be estimated using the drop mass and drop height, but this is the only measurable type of energy in these models. Models that use materials testing systems have attempted to provide energy of fracture measurements from the force-displacement information, but the energies of fracture are not consistent. In posttraumatic OA research, there has not been adequate attention to acquiring fracture energy or energy absorption measurements. Most energy measurements that are reported are the initial gravitational potential energy of impaction. This is surprising, considering the variability between devices could cause inaccuracies in the potential energy measurement. Friction, drag, and other factors could reduce the impact velocity, meaning that not all of the potential energy was converted into kinetic energy pre-impact. Additionally, it is naïve to say that the pre-impact energy is equal to the fracture energy or energy absorbed. During impaction, pre-impact energy could be transferred through a number of different pathways, e.g. specimen damage, soft tissue deformation, vibrations, etc. Even though an accurate measure of fracture energy or energy absorbed has not been focused on in posttraumatic OA research, however, it has been used largely in other areas.

## 1.5 Energy Absorption Measurements

### 1.5.1 Charpy and Izod Impact Tests

Charpy and Izod impact tests were both developed in the early 1900s and are currently American Society for Testing and Materials (ASTM) International methods for determining energy absorption and impact strength [48]. Both tests use a pendulum device that impacts and fractures a specimen. The essential concept of both tests is the same: a pendulum with an initial pre-impact energy impacts and fractures a test specimen, leaving the pendulum with a final post-impact energy (Figure 7).
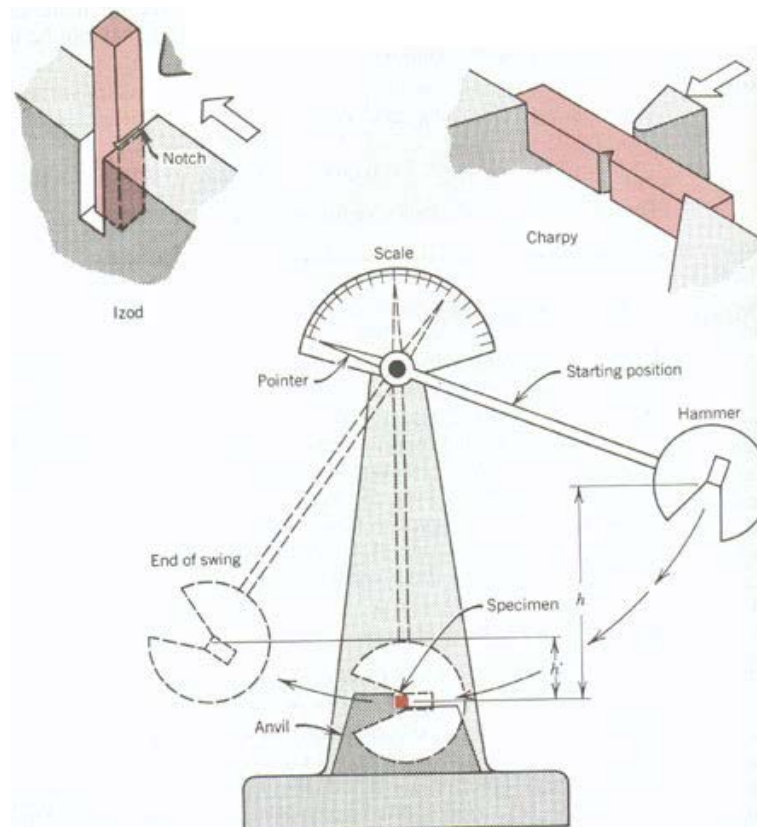


Figure 7:   Schematic illustrating the difference between the Charpy and Izod impact tests. Image adapted and reproduced from Callister [48].

The difference between pre- and post-impact energies is the energy absorbed by the specimen during fracture. The specimens also have standardized dimensions and v-notches for consistent fracture propagation lines. The primary difference between the Charpy and Izod impact tests is the method in which the test specimens are held. The Charpy impact test implements a three-point bending configuration, while the Izod impact test implements a cantilevered beam configuration [48].

### 1.5.2 Abdel-Wahab et al. Izod Impact Test

Recent work by Abdel-Wahab et al. [49] showed the experimental results of an Izod impact test of cortical bone tissue. Some cortical bone specimens were impacted at a low energy level (0.02 joules), while others were impacted at a destructive energy level (0.5 joules). The results showed that the energy absorption measurements were 20% (0.004 joules) of the initial low energy level and 51% (0.256 joules) of the initial destructive energy level. These results were confirmed numerically using extended finite element methods. These results also compared favorably to the Charpy impact test results published by Panagiotopoulos et al. [50]. It appears the Charpy and Izod impact tests are effective for portions of bone tissue, but applying this to an IAF setting *in vivo* might be challenging. Nevertheless, the overall basis of the Charpy and Izod impact tests does confirm that it is naïve, and generally even incorrect, to say that the pre-impact energy is equal to the energy absorbed.

### 1.5.3 Van Zeebroeck et al. Pendulum Device

Van Zeebroeck et al. [51] attempted to measure energy absorbed in impacts of fruits and vegetables using an idea related to the Charpy and Izod impact tests. A pendulum was designed and instrumented with a force sensor, accelerometer, and an optical encoder (Figure 8).
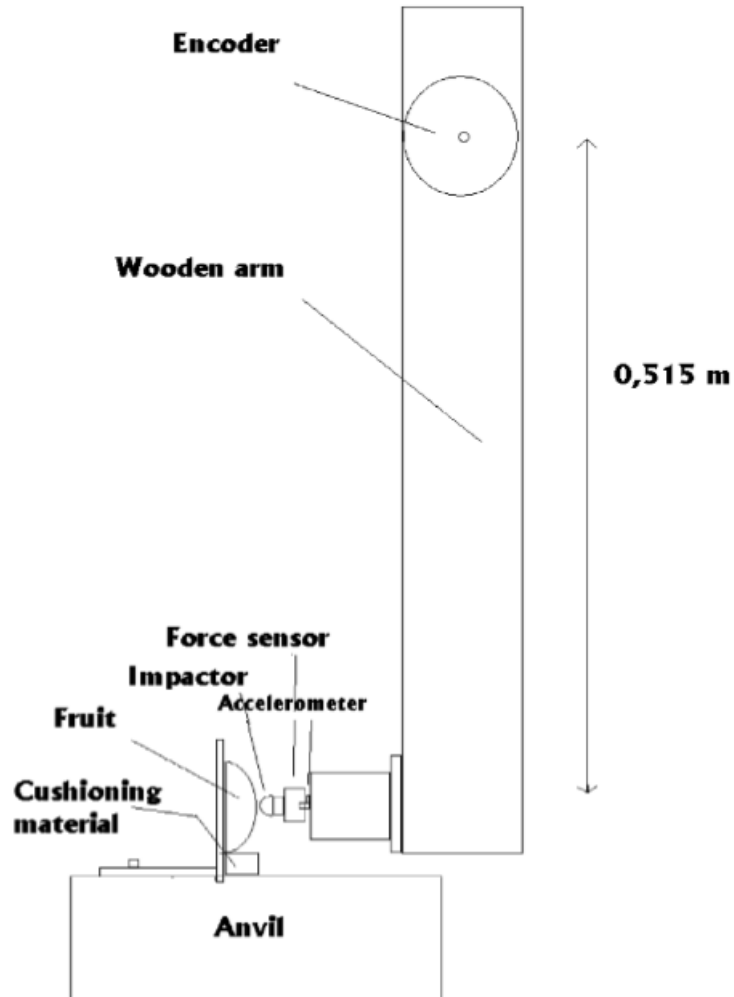
Figure 8: Schematic representation of the pendulum arm with the optical encoder, force sensor, accelerometer, and impacted body ("fruit") are indicated. Image adapted and reproduced from Zeebroeck et al. [51].

The optical encoder, located at the hinge of the pendulum arm, measured the angular position of the pendulum. With the angular position known, the pre- and post-impact kinetic energies could be calculated. As in the Charpy and Izod impact tests, the difference between pre- and post-impact energies was the energy absorbed by the specimen. The utilization of an optical encoder to experimentally calculate the kinetic energy of the pendulum arm provides a more accurate representation of the pre- and post-impact energies when compared to the theoretical potential energy calculations based on

drop height. The kinetic energy calculation is based on the actual pre- and post-impact velocities, while the potential energy calculation takes no account of actually absorbed energy. Furthermore, the optical encoder could ultimately be used to measure the energy absorbed, since the pre- and post-impact kinetic energies were readily available. Even though this particular application of the pendulum device was for impacting fruits and vegetables, instrumenting a blunt impaction or IAF model with an optical encoder seems to be advantageous.

## 1.6 Moving Forward

The information from the literature was important for establishing the initial direction of the IAF model. After reviewing the models present in the literature, the present work of designing, constructing, and evaluating an IAF model began.

CHAPTER 2:  PRIOR DEVELOPMENT OF THE

INTRAARTICULAR FRACTURE MODEL

This chapter discusses the work that was conducted prior to the author's presence. This work established the foundation for the development of the IAF model.

## 2.1 Offset Impaction Technique

A drop tower fracture device was developed that used a compressive impaction technique to produce distal tibial fractures in porcine cadaver legs. These distal tibial fracture patterns were consistent with comparative human ankle fractures created by the same drop tower fracture device (Figure 9). However, the severity of fracture was deemed too severe for usage in future survival studies. In order to maintain a controllable fracture pattern and to reduce the fracture severity for survival study applications, alternative impaction techniques were pursued. A promising method of fracture was found in an offset impaction technique [52]. With the offset impaction technique, the tibia was rotated posteriorly with respect to the compressive force introduced by the drop tower fracture device. This caused the compressive force to be primarily transmitted through the anterior tibial juxta-articular bone. To ensure a consistent fracture pattern, a small stress-rising saw cut (Figure 10) was applied using an oscillating bone saw. The stress-rising saw cut was initiated at the anterior distal tibial surface and proceeded until a thickness of approximately 5-7 millimeters of cancellous bone underlying the articular surface remained intact. While not affecting the articular surface and associated chondrocyte viability, the initial stress-rising saw cut at the anterior distal tibial surface effectively ensured similar fracture line location and orientation after impaction, in a preliminary cadaveric study [52]. Differences in fracture severity from two distinct magnitudes of energy delivery could be seen, yet the fracture patterns still remained consistent (Figure 10). The pattern of chondrocyte damage within these fractures was shown to be analogous to the damage present in the previous human ankle fractures [52,

53]. With the offset impaction technique proving its efficacy in cadaveric studies, it was necessary to alter the specimen mounting procedure to allow for *in vivo* applications. Consequently, much effort and experimentation was consumed in developing a tripod anchorage system that could successfully utilize the discussed offset impaction technique in cadaveric and survival studies.
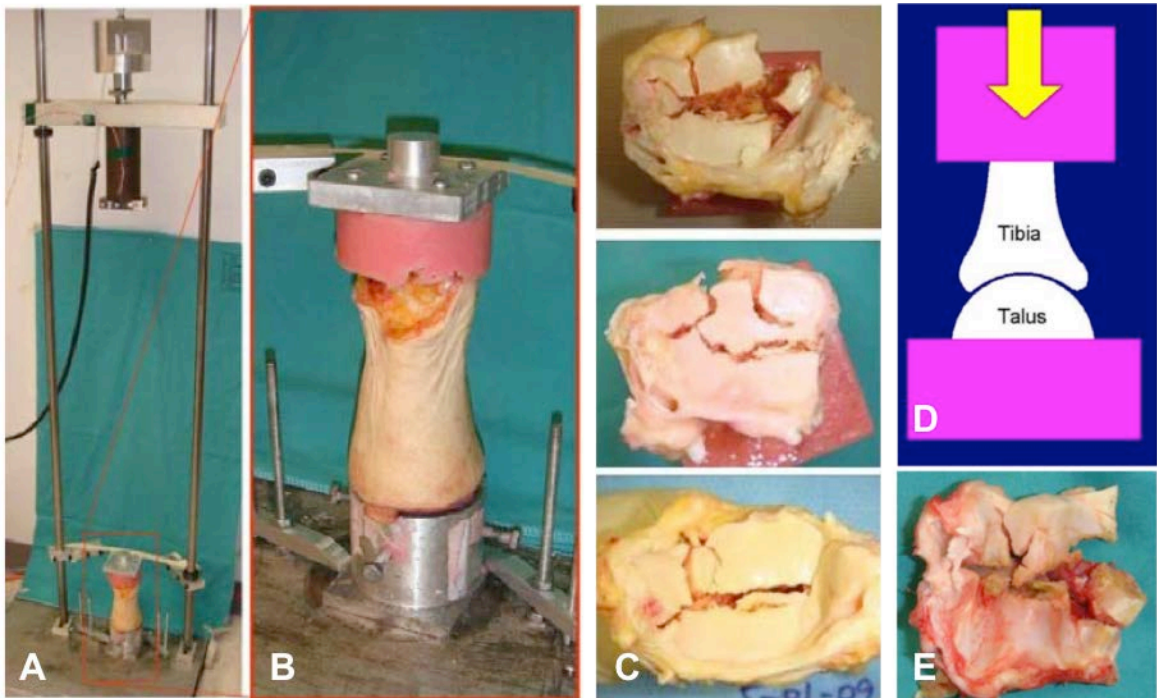


Figure 9:   Drop tower fracture device (A), close-up of a mounted ankle specimen (B), three human ankle fracture patterns (C), schematic of porcine distal tibial fracture technique (D), and a single porcine fracture pattern (E). The fracture patterns between the human and porcine cases were comparable. Note the severity of fracture in the porcine fracture. Images adapted and reproduced from Tochigi et al. [53].
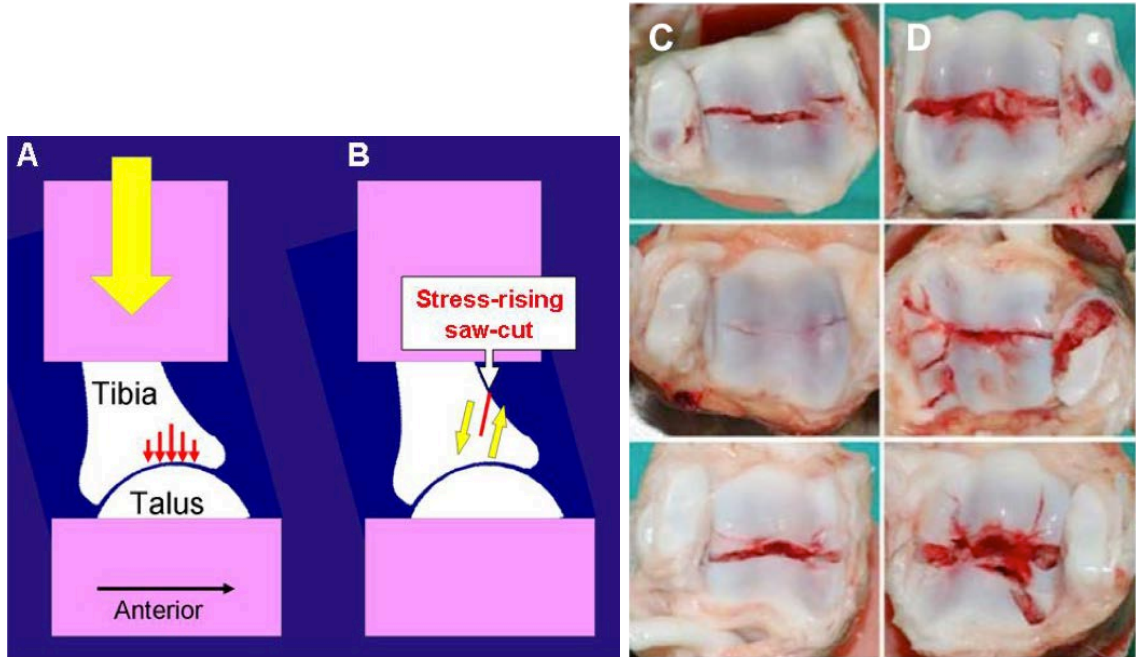
Figure 10: Schematic of the offset impaction insult (A), the introduced stress-rising saw cut technique (B), three fracture patterns from moderate energy impacts (40 joules) (C), and three fracture patterns from high energy impacts (60 joules) (D). The fracture patterns between the compression and offset impactions were comparable. By comparison with Figure 9, note that the severity of fracture in the offset impactions was less than in the compression impactions.

## 2.2 Tripod Anchorage System

A schematic of the tripod anchorage system is shown in Figure 11. The distal tripod pins caused the impact force to be directly transmitted to the talus, which minimized any unwanted energy dissipation via soft tissue during impaction. The distal tibial plate and leg holder shaft maintained the position of the porcine tibia. The distal tibial plate was secured with two pegs and by a cortical screw on the anterior distal tibial surface. The plate contained a ball-in-socket joint that allowed the leg holder shaft to be appropriately aligned with respect to the impact force. The leg holder contained an external fixator pin that was fixed to the proximal tibia, which effectively maintained the position of the tibia. This was important since the offset impaction technique created a

moment during impaction that would tend to rotate the position of the tibia if the tibia was not securely attached to the leg holder.
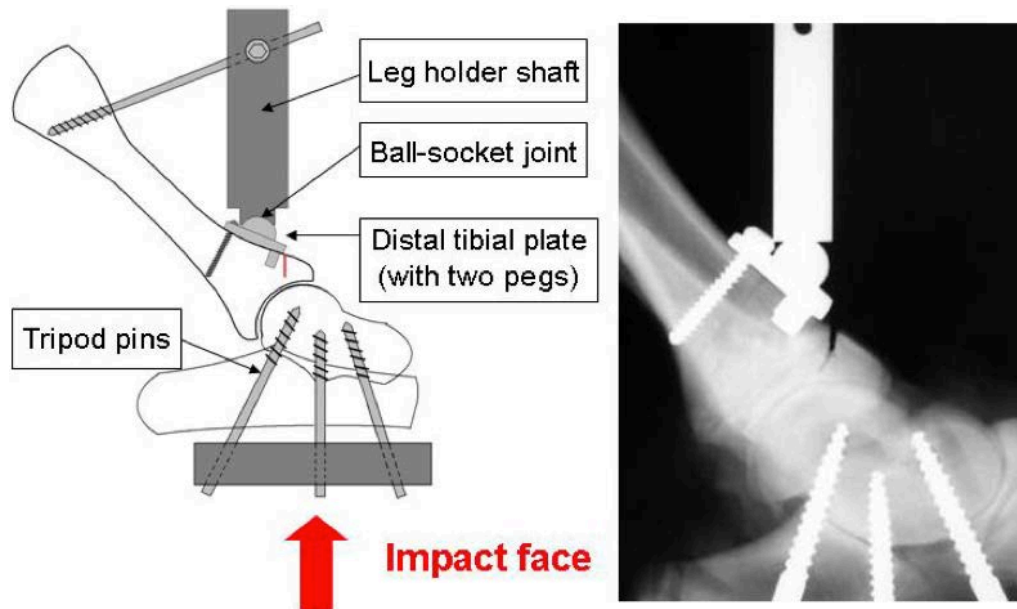


Figure 11:  Schematic (left) and radiograph (right) of the tripod device-to-bone anchorage system. Images adapted and reproduced from Tochigi et al. [52].

Preliminary studies with the drop tower fracture device had tested the tripod anchorage system, using similar techniques as before. The fracture patterns with the tripod anchorage system proved to be comparable to the fracture patterns within the cadaver leg study discussed in the previous section (Figure 12). In addition, the pattern of chondrocyte damage and its time-dependent progression agreed with earlier data from human ankle fractures and porcine cadaver leg study discussed in the previous section (Figure 12). Chondrocyte damage was further investigated using a surgical osteotome as a non-impact osteotomy control to compare results. It was found that for osteotome controls, fractional cell death was significantly lower in the near-edge regions when compared to the impaction fracture joints (Figure 13) [53]. This showed that impaction-

fractured joints experienced greater mechanical stresses than the non-impact osteotomy control joints. Collectively, the preliminary studies that had been performed showed that the offset impaction technique along with the tripod anchorage system was capable of mimicking clinically realistic acute mechanical cartilage damage, in a way that traditional non-impact fracture techniques could not accomplish. Furthermore, the offset impaction technique using the tripod anchorage system appeared to be appropriate for introducing pathophysiologically realistic cartilage injury in future cadaveric and survival studies. However, the drop tower fracture device did not allow live animals to be suitably positioned for anesthesia and surgical management in survival studies. To this end, a pendulum device was developed that incorporated the same offset impaction technique with the tripod anchorage system.
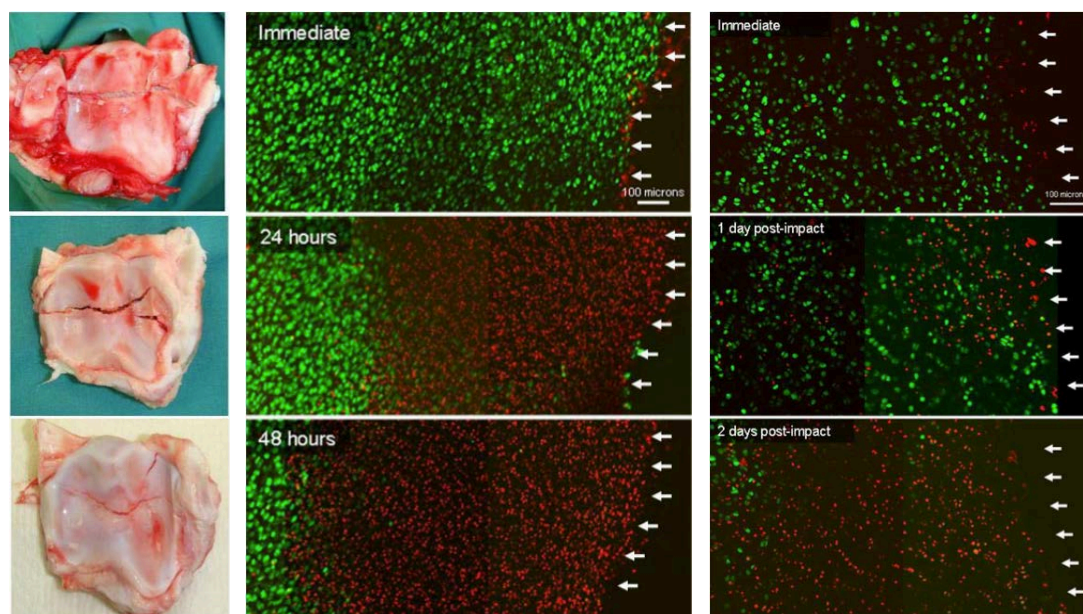


Figure 12: Three fractures created using the tripod anchorage system in the porcine tibia (left). Note the general consistency of fracture line location. Representative time-tracking confocal microscope images at a near-fracture site produced using the tripod anchorage system in the porcine tibia (middle) and using the compressive impaction technique in the human ankle (right). Cells labeled green were alive, while red cells were dead. Arrows indicate the edge of the fragment. Image on right adapted and reproduced from Tochigi et al. [53].
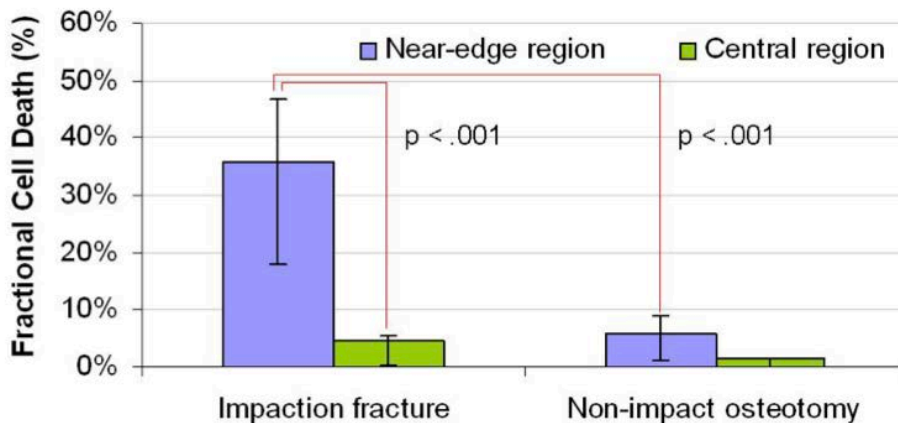
Figure 13: Chondrocyte viability results (2 days post-impact) in impaction-fractured joints vs. non-impact osteotomy controls. Dispersion bars indicate 75th- and 25th-percentile values.

## 2.3 Original Pendulum Device

The original Orthopaedic Biomechanics Laboratory pendulum device is shown in Figure 14. It was built using Computed Numerically Controlled (CNC) machines (a HAAS Tool Room Mill 1 and a HAAS Precision Collet Lathe). The structure was constructed primarily with 6061 aluminum alloy. The pendulum drop mass (3.88 kilograms) was made of 303 austenitic stainless steel alloy.

The energy of impaction could be controlled by adjusting the drop angle (height) of the pendulum arm. A release mechanism was also utilized to consistently release the pendulum arm for impaction. The adjustable support beams allowed the height of the specimen table and pendulum drop mass to be raised or lowered to the desired location. A specimen was positioned according to the offset impaction technique and fixed to the table using the bone-to-device tripod anchorage system.
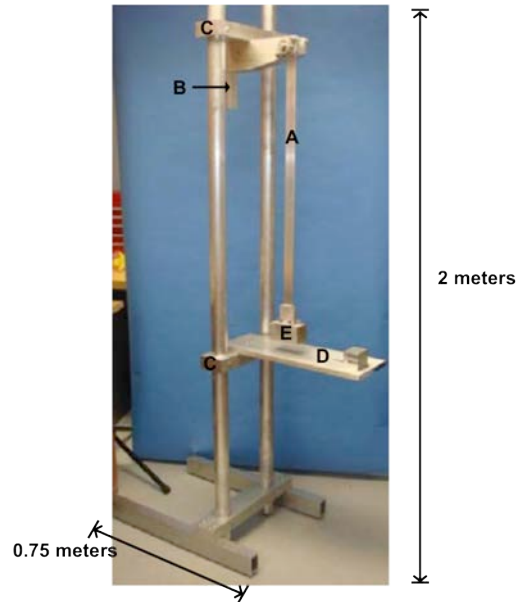
Figure 14:  Original Orthopaedic Biomechanics Laboratory pendulum device. The pendulum arm (A), release mechanism (B), support beams (C), specimen table (D), and pendulum drop mass (E) are shown.


## 2.4 First Application of the Original Pendulum Device

In a pilot study, the pendulum device performed well in creating desirable fracture patterns and inducing progressive chondrocyte damage near the fracture region (Figure 15). These results were comparable with the earlier preliminary studies that had used the drop tower fracture device. Therefore, the pendulum device seemed to be an attractive method to create pathophysiologically realistic cartilage injury in future cadaveric and survival animal studies.

With the general concept established, there was a logical need for quantification. The original Orthopaedic Biomechanics Laboratory pendulum device did not have any type of instrumentation, so the only impaction magnitude value that could be quantified was the pendulum's initial gravitational potential energy (before release). This situation was not a suitable basis for future work, so appropriate instrumentation had to be pursued to accurately measure the amount of energy absorbed by a specimen during fracture

insult. Appropriate modifications and additions necessary to accommodate instrumentation of the pendulum fracture device are discussed in the next section.
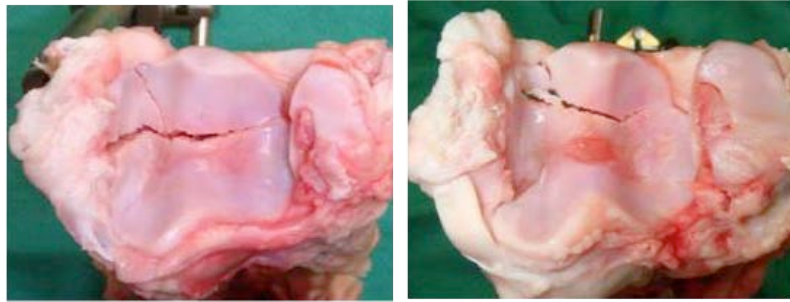


Figure 15: Porcine distal tibia fractures created using the pendulum impaction system.

CHAPTER 3: DEVELOPMENT OF THE PENDULUM

DEVICE AND DATA COLLECTION TECHNIQUE

This chapter discusses the author's contribution to the design of the pendulum device and its instrumentation for collecting energy absorption measurements. Details concerning the appropriate modifications, additional components, and software techniques for ease of data extraction are provided.

### 3.1 Initial Pendulum Instrumentation, Modifications, and Additions

#### 3.1.1 Overview

As with Charpy and Izod impact tests, the energy absorbed by a specimen during fracture was calculated as the difference between pre- and post-impact energy measurements. The instrumentation, modifications, and additions to the pendulum device were centered around this idea. If the pre- and post-impact energies could be accurately measured, then the energy absorption value could be deduced.

Figure 16 shows the general components of the instrumented pendulum device. A brief overview is discussed in this section, while more detail is included in the following sections. The rotary potentiometer measured the angular position of the pendulum arm. The pendulum drop mass was released from a desired drop height. The initial gravitational potential energy was converted into kinetic energy as the drop mass accelerated downward. The pre-impact kinetic energy could be calculated from the rotary potentiometer information. The drop mass impacted the specimen that was rigidly fixed to the low-friction sled on linear bearings. The linear displacement of the sled was calculated from the linear potentiometer, which measured the linear position of the sled. The sled's forward motion was resisted by a coil spring. The stopping mechanism prevented the sled from recoiling after impaction. The sled lever acted as a second-class

lever with the cam follower as the resistive loading point. The post-impact energy could be calculated from the linear potentiometer information and the spring constant.
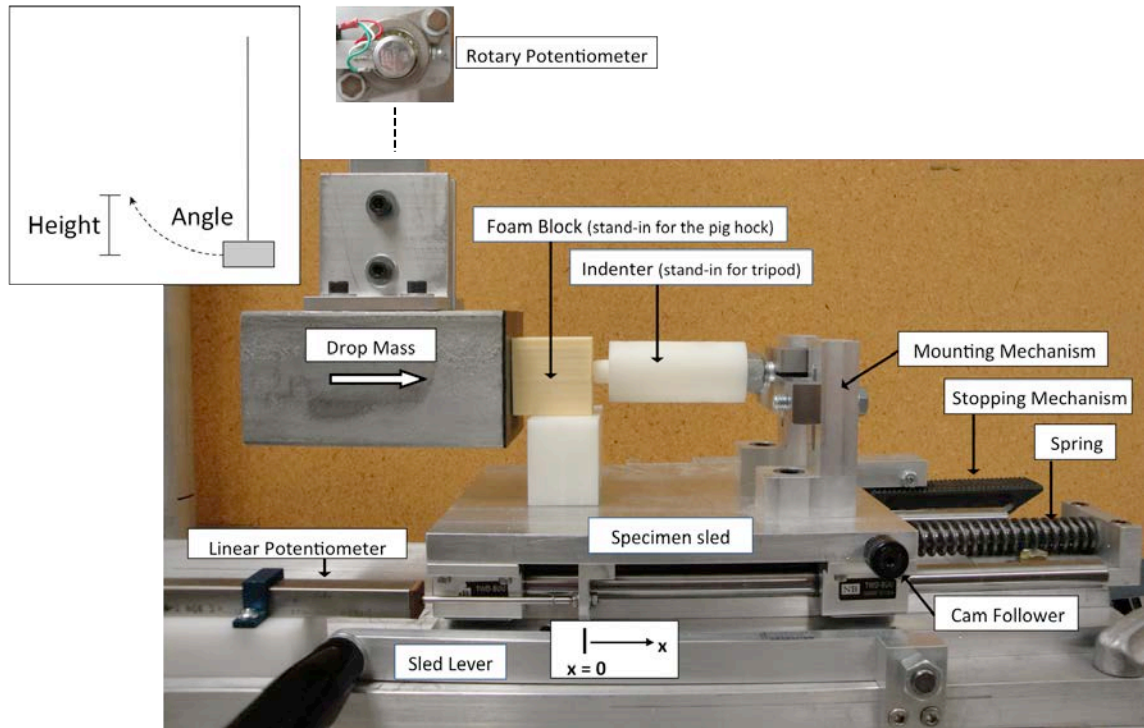


Figure 16: Picture of the general components of the instrumented pendulum device. The angular position (Angle) of the pendulum arm measured by the rotary potentiometer and the linear displacement (x) measured by the linear potentiometer are shown.

### 3.1.2 Rotary Potentiometer

As illustrated by the methodology of Zeebroeck et al. [51], the kinetic energy of a pendulum at the instant just before impact (pre-impact energy) can be measured with an optical encoder located at the hinge of the pendulum arm. This type of measurement technique was attractive for instrumenting the original Orthopaedic Biomechanics Laboratory pendulum device. Ultimately, a rotary potentiometer was attached at the hinge of the original pendulum device. A rotary potentiometer is a three-terminal resistor

with a sliding contact that acts as an adjustable voltage divider. With a given power supply, the voltage output of a rotary potentiometer can range from zero to the given power supply voltage, depending upon the position of the sliding contact. This sliding contact is a rotational sliding contact. Two of the three leads of a rotary potentiometer are for the power supply, while the third lead is for the voltage output. For the voltage output to be meaningful, the rotary potentiometer had to be calibrated. Using a 10-volt power supply, the voltage output of the rotary potentiometer was recorded in 20° increments ranging from 0° to 240°. From this information a calibration curve was fit to obtain a relationship between the voltage output and the angular position of the pendulum arm. With the properly calibrated rotary potentiometer and known pendulum arm length, the angular position of the pendulum arm could be converted into linear position information by implementing basic trigonometry. Since velocity is the derivative of position, the linear velocity of the pendulum drop mass could be computed by finding the slope of the real-time linear position information. The linear velocity could then be used to calculate the kinetic energy of the known pendulum drop mass. The mathematical derivation and corresponding units of the described method are outlined in Equation 2.

Then, the rotary potentiometer could be used to effectively find the kinetic energy of the pendulum drop mass at any time point. Therefore, the pre-impact kinetic energy of the pendulum drop mass could be measured. Given this technique of quantifying the pre-impact energy, a means for quantifying the post-impact energy was also necessary to deduce an energy absorption value. In order to achieve post-impact energy measurement, a sled system was designed and built.

Equation 2:     Equations and variables needed in the derivation and calculation of the pre-impact kinetic energy of the pendulum drop mass.

Equations

$$\theta_{f(t)} = V_{f(t)} C_{rot}$$

$$d_{f(t)} = l_{arm} \theta_{f(t)}$$

$$v = \frac{\Delta d}{\Delta t}$$

$$KE = \frac{1}{2} m v^2$$

Variables

$\theta_{f(t)}$ = angular position of the pendulum arm (relative to the arm's vertical position) as a function of time (in degrees)
$V_{f(t)}$ = voltage output of the rotary potentiometer as a function of time (in volts)
$C_{rot}$ = calibration constant for the rotary potentiometer (in degrees per volts)
$d_{f(t)}$ = linear position of the pendulum drop mass as a function of time (in meters)
$l_{arm}$ = length of the pendulum arm (in meters)
$v$ = linear velocity of the pendulum drop mass (in meters per second)
$t$ = time (in seconds)
$KE$ = kinetic energy of the pendulum drop mass (in joules)
$m$ = pendulum drop mass (in kilograms)

3.1.3 Sled System

The sled system consisted of a low-friction sled on linear bearings, a linear potentiometer, a coil spring, an adjustable mounting mechanism, and a sled lever. Figure 16 provides a visual reference that shows the locations of the sled system components. The low-friction sled sits on linear bearings that allow the sled to move in the same direction as the pendulum drop mass, while restricting motion in the other two directions (vertical and transverse).

The linear potentiometer was attached at the base of the low-friction sled. The linear potentiometer works essentially in the same manner as the rotary potentiometer.

Both are three-terminal resistors with a sliding contact that acts as an adjustable voltage divider. The sliding contact for a linear potentiometer is straight-line, while a rotary potentiometer has a rotational sliding contact. Similar to the rotary potentiometer, the linear potentiometer had to be calibrated in order for the voltage output to be meaningful. Using a 10-volt power supply, the voltage output of the linear potentiometer was recorded in 5-millimeter increments ranging from 0 to 50 millimeters. From this information a calibration curve was fit to obtain a relationship between the voltage output and the linear position of the low-friction sled. With the properly calibrated linear potentiometer, the linear position of the low-friction sled could be found at any time point.

The linear position information alone could not determine the post-impact energy, so a coil spring was introduced. The coil spring was positioned such that the forward motion of the low-friction sled was resisted after impaction. Again, the coil spring had to be properly calibrated to provide meaningful information. Using an MTS 810 materials testing machine (MTS Systems Corp., Eden Prairie, MN), the force required to compress the spring at controlled displacements was recorded in 5-millimeter increments ranging from 0 to 50 millimeters. From this information a calibration curve was fit to obtain the spring constant. With the spring and linear potentiometer, the acquired spring constant and the linear position information of the low-friction sled could be used to calculate the spring energy required to stop the low-friction sled's forward progress (post-impact energy). This energy is the potential energy that is stored in the spring when it is compressed by the low-friction sled. To avoid confusion with the initial gravitational potential energy of impaction, the energy described will be referred to as "sled energy" for the remainder of this work. The equation used to calculate the sled energy from the spring constant and the linear position information of the low-friction sled is outlined in Equation 3. The linear displacement of the low-friction sled was equivalent to the compressive length of the spring, because the spring was initially at its equilibrium

position (not prestressed), and the spring and the low-friction sled were in intimate
contact.

Equation 3:     Equation and variables needed to calculate the post-impact sled energy.

Equation

$$SE = \frac{1}{2}kx^2$$

Variables

$SE$ = sled energy (in joules)
$k$ = spring constant (in newtons per meter)
$x$ = forward displacement of the sled (relative to the sled's original resting position)
   (in meters)

The sled system also needed a method for attaching the tripod anchorage system
used in the offset impaction technique for creating IAFs. To this end, an adjustable
mounting mechanism was rigidly fixed to the low-friction sled. The mounting mechanism
allowed the tripod anchorage system to be adjusted in the direction of the pendulum drop
mass, as well as the vertical direction. Adjustability in the transverse direction was not
allowed, since it was deemed unnecessary.

Due to the intrinsic behavior of a spring, there would be recoil after release of the
compressing force compressed. In an attempt to minimize this effect, a stopping
mechanism was designed and built. The stopping mechanism was a simple ratchet
mechanism that allowed movement in the direction of impact or compression, but that
halted any movement in the opposite direction (direction of recoil).

Since the stopping mechanism would need to be released to return the spring to its
equilibrium position, a sled lever was attached for assistance. A cam follower was

attached to the low-friction sled to provide a point of contact between the sled and sled lever. The dimensions of the sled lever, along with the location of the cam follower and sled lever, generated a mechanical advantage of 6. This was more than enough for easy operation of the sled lever.

### 3.1.4 Data Collection Components

The analog voltage outputs of the potentiometers needed to be digitized and collected on a computer to calculate the energy measurements. A power supply, analog-to-digital (A/D) converter, and computer had to be available to collect impaction data from the potentiometers. For initial trials with the pendulum device, a dual-output power supply (Model #E3620A, Agilent Technologies Inc., Santa Clara, CA) was used to supply 10 volts to each of the two potentiometers. The dual-output power supply also had a panel meter that displayed the output voltage of a selected potentiometer. An NI USB-6210 (National Instruments Corp., Austin, TX) A/D converter was used with a Dell XPS laptop (Dell Inc., Round Rock, TX) to collect the voltage output readings from the potentiometers. To minimize the amount of unwanted data, a 3-volt AC powered hand trigger was used. This particular trigger voltage was chosen because 3 volts is an effective voltage for digital triggers—digital triggers require a transistor-to-transistor logic (TTL) voltage level of 1-5 volts.

The pendulum device and the additional components could collect position data from the rotary and linear potentiometers. From these data, the pre-impact kinetic energy of the pendulum drop mass and the post-impact sled energy could be calculated. The energy absorbed by the specimen during impaction could then be calculated as the difference between the pre-impact kinetic energy and the post-impact sled energy (Equation 4).

Equation 4:    Equation and variables needed to calculate the energy absorption during
               fracture.

Equation

$$EA = KE - SE$$

Variables

$EA$ = energy absorption during fracture (in joules)
$KE$ = pre-impact kinetic energy (in joules)
$SE$ = post-impact sled energy (in joules)

## 3.2 Final Pendulum Instrumentation, Modifications, and

## Additions

Once the initial pendulum instrumentation, modifications, and additions were
completed, many preliminary impaction trials were conducted to find aspects that needed
improvement. The preliminary impaction trials and the variables that were tested can be
seen in Table A1 in the Appendix. This section discusses the development phase for each
major component. Topics covered include preliminary impaction results, failure
modalities, modifications, reasoning for modifications, and fine-tuning.

### 3.2.1 Rotary Potentiometer

Figure 17 shows the rotary potentiometer attached at the hinge of the pendulum
arm. After preliminary impactions were conducted, the rotary potentiometer proved to be
quite sufficient. The signal from the rotary potentiometer was relatively noise-free, so
calculating the slope of the linear position information was not problematic. Based on the
information from the rotary potentiometer, it was clear that the linear velocity of the
pendulum monotonically increased until the event of impaction, such that the maximum
linear velocity occurred at the point of incipient impaction. Logically, this would be
expected to happen, because the pendulum drop mass was accelerating during the

downward swinging motion. Since the maximum linear velocity could be found with relative ease, the pre-impact kinetic energy was also easily calculated. Based on the initial impaction results, the pre-impact kinetic energy was approximately 93% of the pendulum's pre-release gravitational potential energy. This was reasonable, in that the pre-impact kinetic energy was expected to be less than the initial gravitational potential energy due to friction, drag, and other factors that would decrease the linear velocity of the pendulum drop mass. Since the signal from the rotary potentiometer was relatively easy to work with and since the magnitude of the pre-impact kinetic energy measurements seemed to be very reasonable, the rotary potentiometer was deemed to need no further modifications. The original rotary potentiometer was therefore used throughout future impactions.
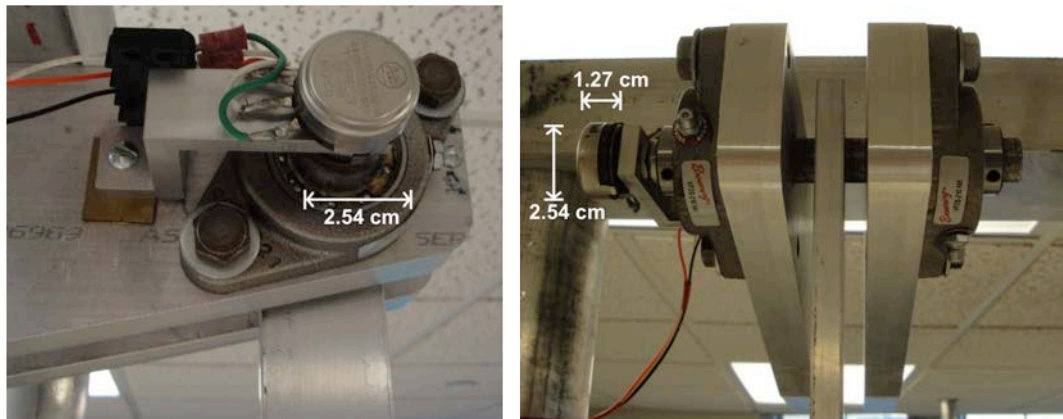


Figure 17:  Side view (left) and front view (right) of the rotary potentiometer attached to the hinge of the pendulum arm.

### 3.2.2 Linear Potentiometer

Figure 18 shows the original linear potentiometer that was attached to the low-friction sled. Unlike its rotary counterpart, the linear potentiometer caused concerns even before preliminary impactions. The sliding contact had a significant amount of drag in

some positions of its traverse. In addition to the drag issue, the original linear

potentiometer only accommodated 6.1 centimeters of traverse. Depending on the

impaction magnitude, this amount of travel sometimes exceeded this distance, causing

the linear potentiometer to be bottomed out. Bottoming out a potentiometer obviously is

undesirable, for multiple reasons. To start with, if the maximum travel were reached

during an impaction, the sled energy information would be incorrect. The measured

compression distance would be too low, leading to a subsequent under-report of post-

impact sled energy. In addition to measurement inaccuracies, bottoming out could have

damaging effects to the potentiometer itself.
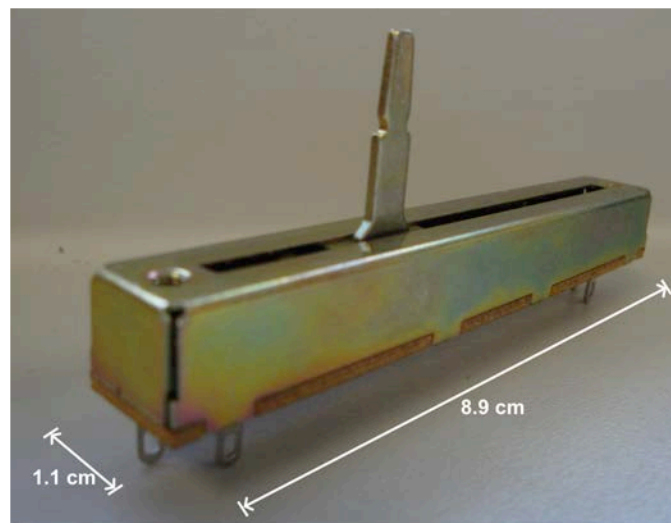


Figure 18: Original linear potentiometer that was attached to the low-friction sled.

Therefore, a new linear potentiometer was investigated (Figure 19). The drag

from the new sliding contact was insignificant when compared to that from original linear

potentiometer. This resulted in smoothly accurate linear displacement readings. The new

linear potentiometer also allowed for a linear travel up to 15.2 centimeters, almost a

150% increase when compared to the original linear potentiometer. This would prevent

any of the problems associated with bottoming out the potentiometer. To calibrate the voltage output signal of the new linear potentiometer, again a 10-volt power supply was used. The voltage output was recorded in 5-millimeter increments ranging from 0 to 65 millimeters. Again, this information was used to fit a calibration curve and obtain a relationship between the voltage output and the linear position of the low-friction sled. Once the new linear potentiometer was calibrated and properly attached to the low-friction sled, preliminary impactions were conducted. The signal from the linear potentiometer was still not as "clean" as that from the rotary potentiometer. However, the magnitude of the noise was not large enough to cause problems with measuring the linear displacement. Plus, simple signal processing techniques could always be applied to filter out the unwanted noise frequencies. With the drag being insignificant, the travel being more than sufficient, and the signal being relatively clean, the new linear potentiometer was deemed adequate for use in future impactions, and no further modifications had to be made.
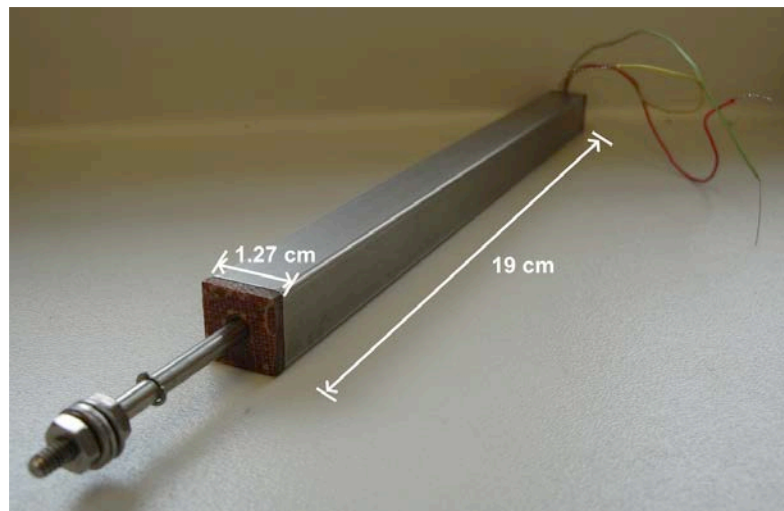


Figure 19: New linear potentiometer that was attached to the low-friction sled.

3.2.3 Low-Friction Sled and Linear Bearings

Figure 20 shows the original low-friction sled and linear bearings. The original low-friction sled and linear bearings were part of another device, so they were used temporarily as proof of concept. Nevertheless, its temporary use contributed to the design process of the definitive low-friction sled and linear bearings. Initial observations revealed that minor surface defects (corroded shaft with support rail) contributed to a slight increase in friction that could affect the post-impact sled energy measurements.
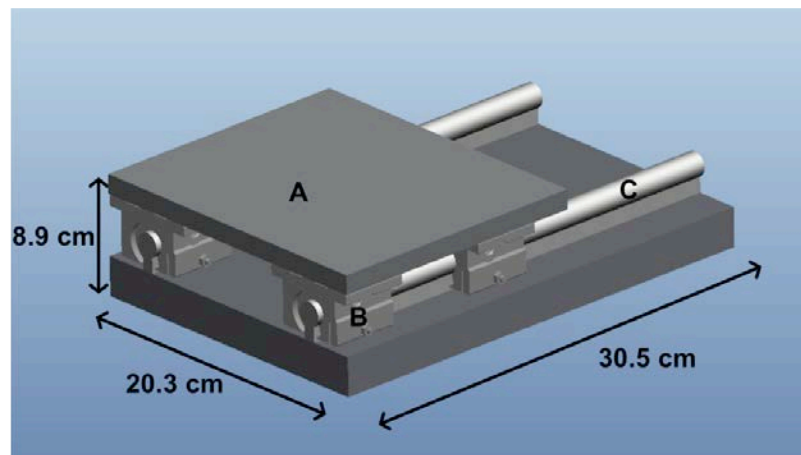


Figure 20:  Schematic of the original low-friction sled (A), linear bearings (B), and shafts with support rails (C).

Trial impactions showed that a low-friction sled and linear bearings could in principle be effectively used for the desired application. Post-impact sled energies could be gathered, and their magnitudes seemed reasonable. No insurmountable difficulties arose during trial impactions that indicated need to abandon the essential concept. With the proof-of-concept established, a new low-friction sled and linear bearings needed to be procured to replace the temporary version.

Figure 21 shows the new low-friction sled and linear bearings. The sled table was built from 6061 aluminum alloy using a HAAS Tool Room Mill 1. Linear sleeve open bearings (Part #6374K314, McMaster-Carr, Elmhurst, IL) were purchased and fixed to the underside of the sled table and aligned with a purchased shaft with support rail (Part #6557K22, McMaster-Carr, Elmhurst, IL).

Preliminary impactions with the new low-friction sled and linear bearings exhibited slight improvement from its original counterpart. Post-impact sled energies were gathered, and their magnitudes were similar to those of the original unit. Through manual observation, the frictional component of the new bearings was less than that of the previous bearings. This was probably attributed to the pristine condition of the new components, specifically the non-corroded surface of the shaft with support rail. From the preliminary impactions and observations, the new low-friction sled and linear bearings could successfully be used in future impactions.
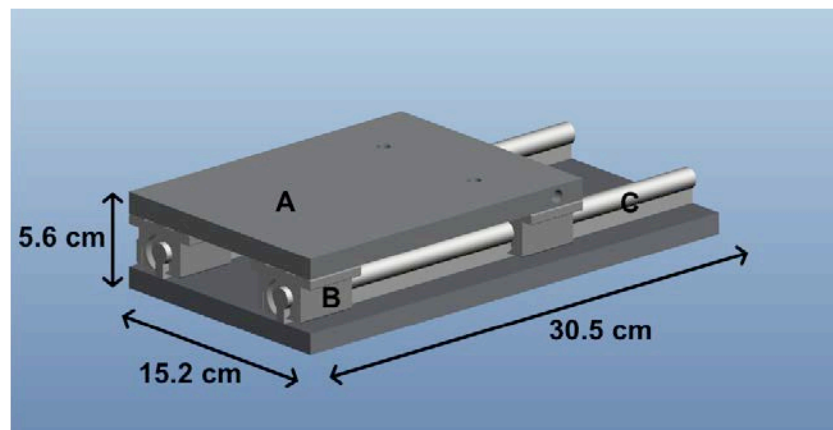


Figure 21:  Schematic of the new low-friction sled (A), linear bearings (B), and shafts with support rails (C).

3.2.4 Adjustable Mounting Mechanism

The original adjustable mounting mechanism can be seen in Figure 22. The mounting mechanism had slotted holes that allowed the tripod anchorage system to be adjusted in the direction tangent to the pendulum drop mass arc, as well as in the vertical direction. When the original mounting mechanism was applied to *in vivo* cases, more adjustability was found to be needed for most animals. The adjustability in the direction of the pendulum drop mass was more than sufficient, but more adjustability was often needed in the downward vertical direction. Due to it being coupled to the overall body of the animal, the hock could not be rotated with ease, unlike the case for the cadaveric leg (limb-only) impactions. This caused the need for adjustability in the transverse direction.
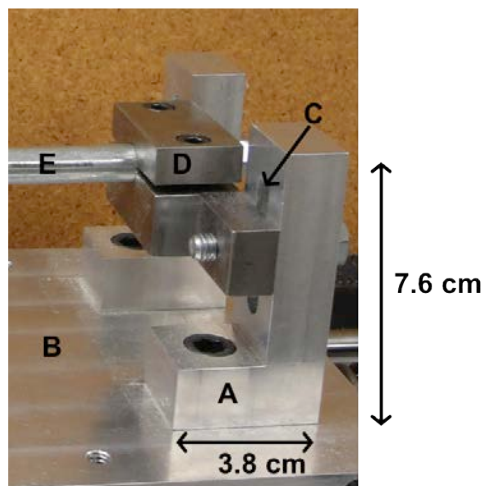


Figure 22:  Original adjustable mounting mechanism (A) rigidly fixed to the low-friction sled (B). The slotted holes (C) allowed for vertical movement. The clamp (D) allowed the leg holder shaft (E) to be adjusted in the direction tangent to the pendulum drop mass arc.

To allow for the added adjustability, the original mounting mechanism was modified (Figure 23). The modified mounting mechanism trimmed off excess material that was limiting the full range of adjustability in the downward direction. These

modifications allowed the tripod anchorage system to be adjusted downward an additional 2.5 centimeters. The modified mounting mechanism also included a different plate, with slotted holes that allowed for adjustability transversely approximately ±1.9 centimeters. Following additional *in vivo* trials, excess material was trimmed off the newly-added plate. This final modification was made because the new plate would occasionally make contact with particularly large animals. The final modification did not pose the same problem in future *in vivo* cases, even with the overweight specimens.
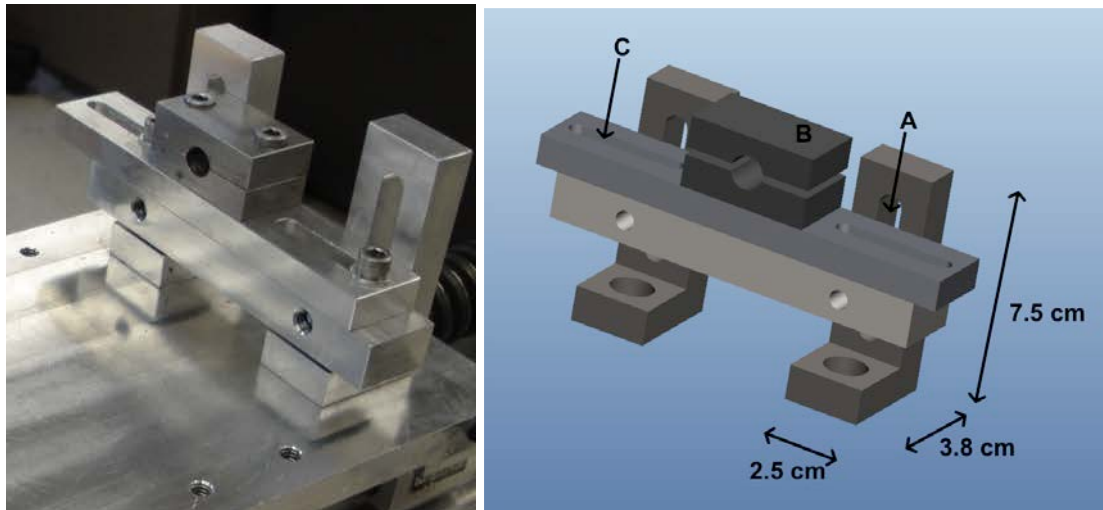


Figure 23:  Picture (left) and schematic (right) of the modified adjustable mounting mechanism. The original slotted holes (A) and clamp (B) remained. The additional set of slotted holes (C) allowed for transverse movement.

## 3.2.5 Stopping Mechanism

The stopping mechanism allowed movement in the direction of impact or spring compression, but halted any movement in the opposite direction. The original stopping mechanism is shown in Figure 24. Initially, it was felt to be desirable to minimize the recoil of the spring, in an attempt to prevent additional damage to the specimen. However, after analyzing high-speed video data (Oqus Camera Series, Qualisys AB,

Gothenburg, Sweden), the recoil of the spring was found not to be aggressive as presumed. In fact, the recoil was quite smooth, gentle, and non-destructive to the specimen. Given this additional information, the idea of the stopping mechanism was reevaluated. In preliminary impactions, the original stopping mechanism was not always successful in halting movement in the opposing direction. Sometimes the stopping mechanism would bounce back in a skipping manner, which caused a jerking motion of the specimen. Even when the stopping mechanism was successful, other concerns emerged. Due to the ratchet nature of the stopping mechanism, it inherently produced friction during forward movement. This would cause the linear displacement of the low-friction sled to decrease, and the subsequent post-impact sled energy to be erroneously low. In addition, the stopping mechanism protruded in such a fashion there was contact with the specimens *in vivo*. That contact led to substantially lower linear displacement and thus post-impact sled energy measurements. From the observations of its shortcomings, the stopping mechanism did not prove to be advantageous in any way. Although the stopping mechanism seemed beneficial in theory, in practice it did not perform as planned. Ultimately, this component was removed from the pendulum device, in the interest of making more accurate measurements.
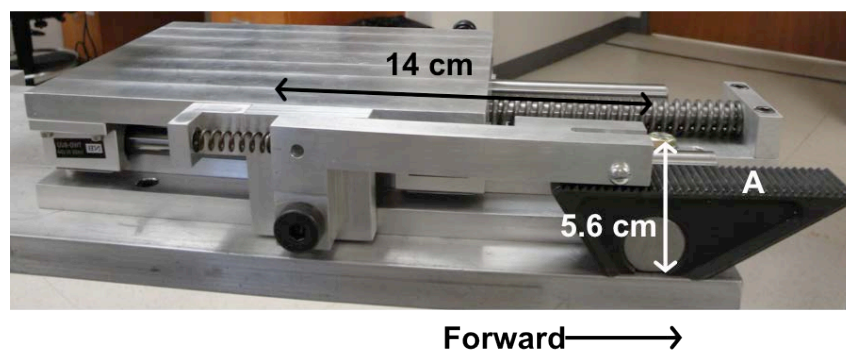


Figure 24:  Original stopping mechanism that allowed sled movement forward, but disallowed movement in the reverse direction. The teeth (A) of the stopping mechanism allowed for the ratcheting behavior.

## 3.2.6 Sled Lever

The location of the sled lever with respect to the low-friction sled and the cam follower can be seen in Figure 25. With the stopping mechanism removed, the original purpose of the sled lever was not applicable. However, secondary functions of the sled lever arose during preliminary tests. While setting up the pendulum device for data collection, it was desirable to test the potentiometers first to ensure accuracy. In order to test the linear potentiometer, the coil spring had to be compressed for the low-friction sled to move in the direction of the pendulum drop mass. Compressing the spring by hand was possible, but extremely difficult when the compression displacement was large. When the sled lever was attached, it allowed the user to maneuver the sled and coil spring with relative ease. Even though the original purpose of the sled lever was not applicable with the stopping mechanism removed, the secondary function of enabling testing of the linear potentiometer prior to impaction was still important. Therefore, the sled lever and cam follower remained in their original positions for future impactions.
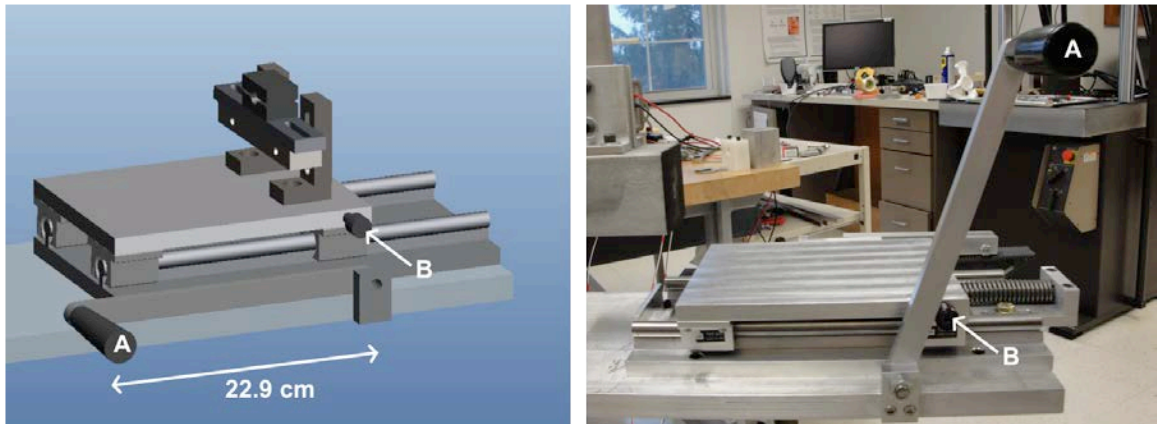


Figure 25:  Schematic (left) and picture (right) showing the locations of the sled lever (A) and cam follower (B). The schematic shows the lever position at rest, and the picture shows the lever position when it is in use.

### 3.2.7 Coil Spring

Figure 26 shows the progression of coil springs that were used for the pendulum device. The respective spring constants, maximum compression displacements, and total energy capacities are shown in Table 1. The first spring was chosen for low-energy impaction tests initially. After it became apparent that the energy capacity of the first spring was too small for fracture, it was replaced with the second spring. The second spring performed well when impacting surrogate specimens, but preliminary impactions with cadaver leg porcine hock specimens and the first *in vivo* specimen raised concern. The compression displacement limits were neared frequently, so the energy capacity of the second spring was being reached. This would cause inaccurate post-impact sled energy readings and could damage the spring. So again, the spring had to be replaced. The third spring performed very well in preliminary impactions with cadaver leg porcine hock specimens. When transitioning to *in vivo* trials, the third spring initially showed promise. However, its energy capacity started being approached when the stopping mechanism was removed. From all the information that was gathered, it was decided that the next spring should err on the "safe side" for possible energy capacity. To that end, the fourth spring allowed for an energy capacity that neared the amount of pre-impact kinetic energy. This was felt to be sufficient to allow for any plausible changes that might have been made to the device or surgical procedure. The larger energy capacity also allowed for the possibility of impacting specimens other than porcine hocks in the future, perhaps requiring higher energy capacity values. From *in vivo* impactions with the fourth spring, the results were consistent and did not approach the spring's energy capacity. The preliminary results were very encouraging and showed that the fourth spring could effectively be used for future impactions.
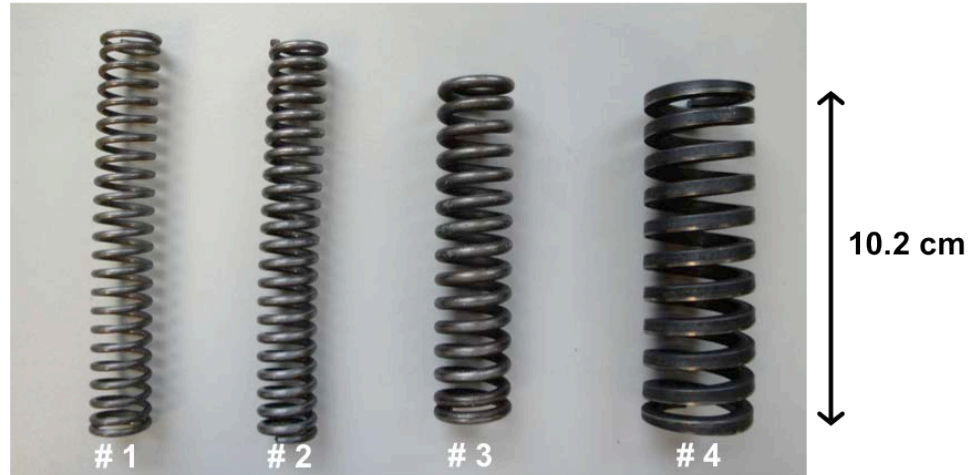
Figure 26: Progression of the coil springs that were used for the pendulum device. The first spring is seen at the far left, progressing to the fourth and final spring on the far right.

Table 1: The characteristics for the progression of coil springs, including the respective spring constants, maximum compression displacements, and total energy capacities.

| Spring # | Spring Constant (N/mm) | Maximum Compression (mm) | Energy Capacity (J) |
|---|---|---|---|
| 1 | 3.2 | 71.4 | 8.2 |
| 2 | 11.2 | 50.4 | 14.2 |
| 3 | 20.6 | 44.6 | 20.4 |
| 4 | 36.7 | 47.2 | 40.9 |

3.2.8 Data Collection Hardware

The original data collection hardware and the cart that was used to house that hardware can be seen in Figure 27. This configuration required many cords to connect from the pendulum device, to the cart, and finally to an outlet. When maneuvering the pendulum device and hardware cart during preliminary *in vivo* impactions, it was difficult

to protect the cords. Attention had to be paid so that the hardware cart would not run over the cords. If the cart and pendulum device needed to be appreciably separated from each other, the cords would be stretched. Overall, the configuration led to awkward and stressful mobility issues. To keep the hardware more organized and connected, it was desirable for the hardware to be attached to the pendulum device in some manner. To accommodate for such attachment, two shelves were constructed from Delrin.
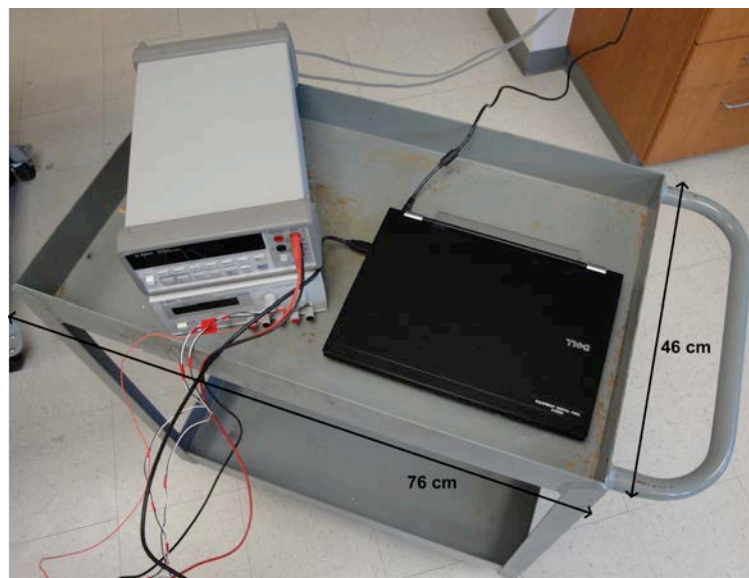


Figure 27:  Original data collection hardware and cart with wires extending to connect to the potentiometers and an available outlet.

Also, the previous dual-output power supply could only be used temporarily, because it was needed for other purposes. The new hardware that was purchased to replace the previous dual-output power supply consisted of two 10-volt power supplies (Part #PSS-10, Omega Engineering Inc., Stamford, CT), a panel meter (Part #DP41-E, Omega Engineering Inc., Stamford, CT), and a rotary selector switch (Part #65865K32, McMaster-Carr, Elmhurst, IL). The two 10-volt power supplies had the same functionality as the original dual-output power supply in terms of providing the

potentiometers with 10-volt excitation voltages. The panel meter also had the same functionality as that in the original dual-output power supply, in displaying the voltage outputs of the potentiometers. When compared to the original dual-output power supply, the rotary switch was an improvement for purposes of checking the voltage drops across different components. With the original dual-output power supply, two electrical lead hook clips had to be placed properly across a single component to view its corresponding voltage drop. The hook clips had to be repositioned each time a different component was of interest. When replaced with the rotary switch, each component's voltage drop could be viewed by simply changing the position of the rotary switch. Components to be checked were the two power supplies and the two potentiometers. Before each impaction, the voltage drops across the 10-volt power supplies were confirmed. Additionally, the voltage drop across the linear potentiometer was checked to ensure that no inaccuracies arose. Finally, the voltage drop across the rotary potentiometer was of primary interest. The initial vertical position had to be confirmed for proper computation of the pre-impact kinetic energy of the pendulum drop mass. It was also required to view the voltage output of the rotary potentiometer, in order to set the appropriate drop angle (energy input) of impaction. With the rotary switch attached, cycling through each desirable component was much easier and more intuitive than using the previous dual-output power supply. The two power supplies, panel meter, and rotary switch were all wired and fixed to the Delrin shelves once their functionalities were confirmed in preliminary impactions.

In the same preliminary impactions, the original A/D converter and laptop performed well in collecting the voltage output readings from the potentiometers. There was no need for alterations, so they were also fixed to the Delrin shelves. The 3-volt AC powered hand trigger that was used worked well, but required an additional operator. In an attempt to keep the required operator numbers to a minimum, a 3-volt foot trigger replaced the hand trigger. This allowed the same operator to trigger the data collection and release the pendulum drop mass, effectively reducing the amount of required

operators to one. The foot trigger was also powered with two AA batteries to eliminate the need for an AC power connection. With successful implementation of the foot trigger, it remained on the pendulum device for future impactions. The final configuration of the data collection hardware fixed to the Delrin shelves of the pendulum device can be seen in Figure 28. The corresponding circuit diagram can be seen in Figure A1 in the Appendix.
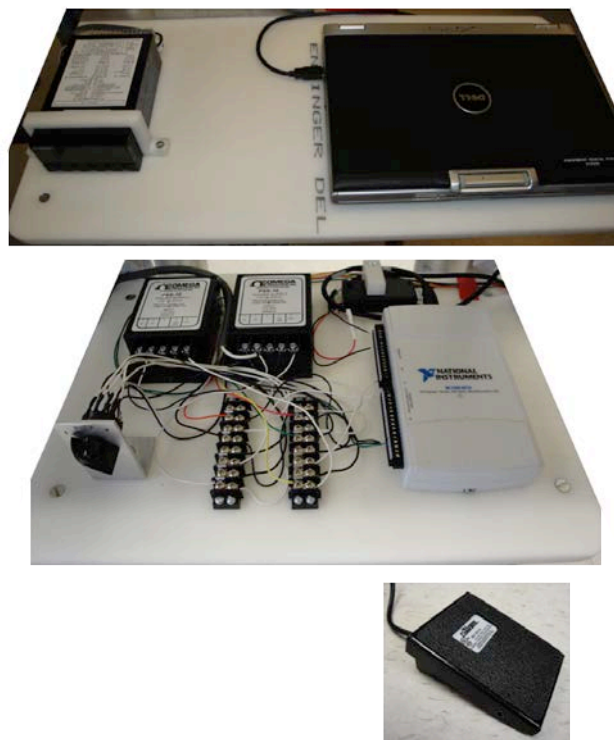


Figure 28: Final configuration of the data collection hardware fixed to the Delrin shelves. The top shelf contained the panel meter for easy viewing, and afforded ease of accessibility of the laptop computer. The bottom shelf contained the two power supplies (in the rear) that power each of the potentiometers, the battery pack for the foot trigger located (in the rear), the rotary switch on the left that cycled through each voltage output, two terminal blocks (in the front) for circuit organization, and the A/D converter (on the right). The foot trigger was placed at a desirable location on the floor by the user.

### 3.2.9 Pendulum Arm Modifications

The original pendulum arm had a thickness of 4.8 millimeters, which resulted in undesired transverse movement that could cause an indirect impact. To alleviate this problem, the pendulum arm thickness was increased to 9.5 millimeters, resulting in a 700% increase in the area moment of inertia when compared to the original arm thickness. Preliminary impactions further reaffirmed that the tendency of the pendulum arm to move transversely was greatly decreased with the thicker pendulum arm.

Preliminary impactions also indicated the need for a greater pendulum drop mass. The original pendulum drop mass (3.88 kilograms) only allowed for a maximum pre-impact energy of approximately 38 joules at a drop angle of 90°. Larger pre-impact energies were found to be required for fractures *in vivo*, so the pendulum drop mass was increased to 5.82 kilograms. The larger pendulum drop mass allowed for a maximum pre-impact energy of approximately 57 joules at a drop angle of 90°, an effective increase of 50%. In preliminary *in vivo* fractures, the larger pendulum drop mass was successful in consistently creating fractures, while the smaller proved insufficient for fracture.

### 3.2.10 Stability Modifications

Finally, modifications were made that improved the stability of the pendulum device during impaction. Preliminary *in vivo* trials showed that the overall stability of the pendulum device was not sufficient for controlled impactions. Noticeable problems included the entire pendulum device sliding forward in the direction of the pendulum drop mass, tilting up on its front two feet, and bowing forward during impaction. To prevent the pendulum device from sliding forward on the floor, the feet were replaced with larger ones that were made of rubber (Figure 29). The larger surface area and usage of rubber material provided more friction on the floor, and successfully prevented any forward sliding in the direction of the pendulum drop mass. To prevent the pendulum device from tilting up on its front two feet, three 25-pound (11.3-kilogram) weights were

attached to the rear (Figure 30). This solved the pendulum tilting problem in preliminary

impactions, and of course more weight could always be added if needed. To prevent the

pendulum device from bowing forward, cross supports were attached to the rear as well

Figure 31. This modification was the main source of improved structural stability. With

these stability modifications in place and tested, the pendulum device was finally ready to

be put to use in actual *in vivo* impaction studies. The final pendulum configuration is

shown in Figure 32 and Figure 33. Before describing the actual impaction studies and

results, however, the data collection technique needs to be set forth.



Figure 29: Original smaller feet (2.54 centimeter diameter) with metal bottoms and the new larger feet (5.08 centimeter diameter) with rubber bottoms. The pictures on the left are for composition comparison. The picture on the right is for size comparison.
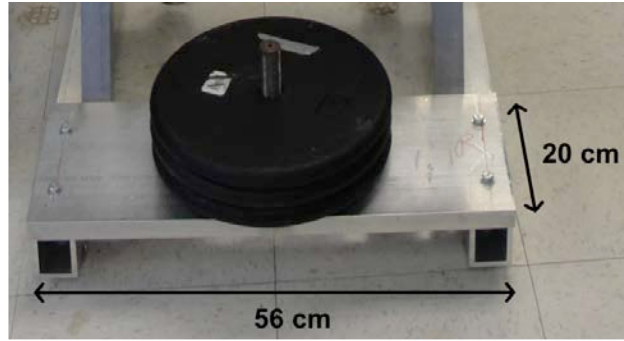
Figure 30: Three 25-pound (11.3-kilogram) weights attached to the rear of the pendulum device for added stability. Weight could be added or removed as needed.
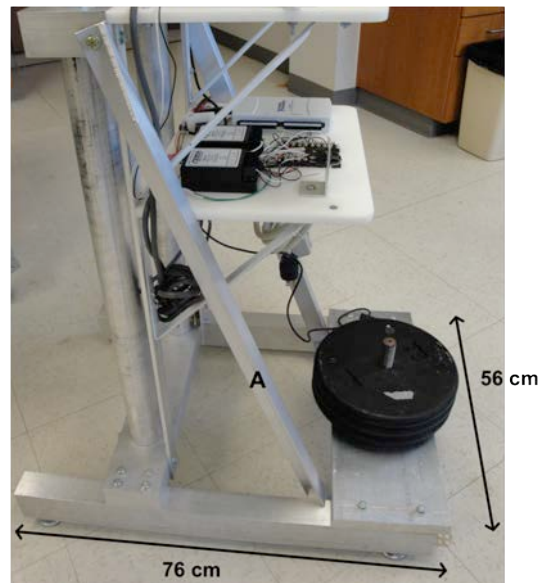


Figure 31: Cross-supports (A) from the top left to the bottom right of the device. These additional supports provided a substantial increase in stability during impactions.
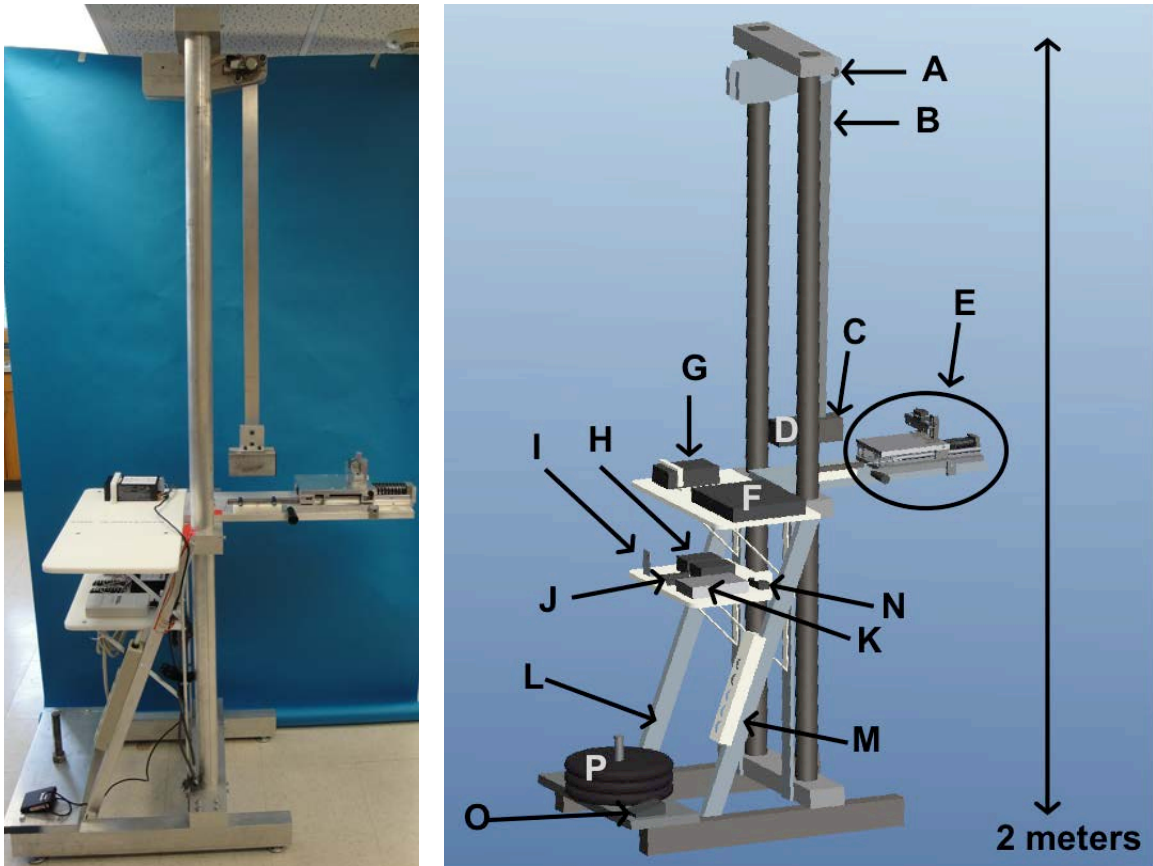
Figure 32: Picture (left) and schematic (right) of the finalized pendulum device. The schematic shows the rotary potentiometer (A), pendulum arm (B), original pendulum drop mass (C), additional pendulum drop mass attached (D), sled components (E), laptop (F), panel meter (G), power supplies (H), rotary switch (I), terminal blocks (J), A/D converter (K), cross supports (L), power strip (M), battery (N) powering the foot trigger (O), and weights (P). The laptop and weights are not pictured on the left.
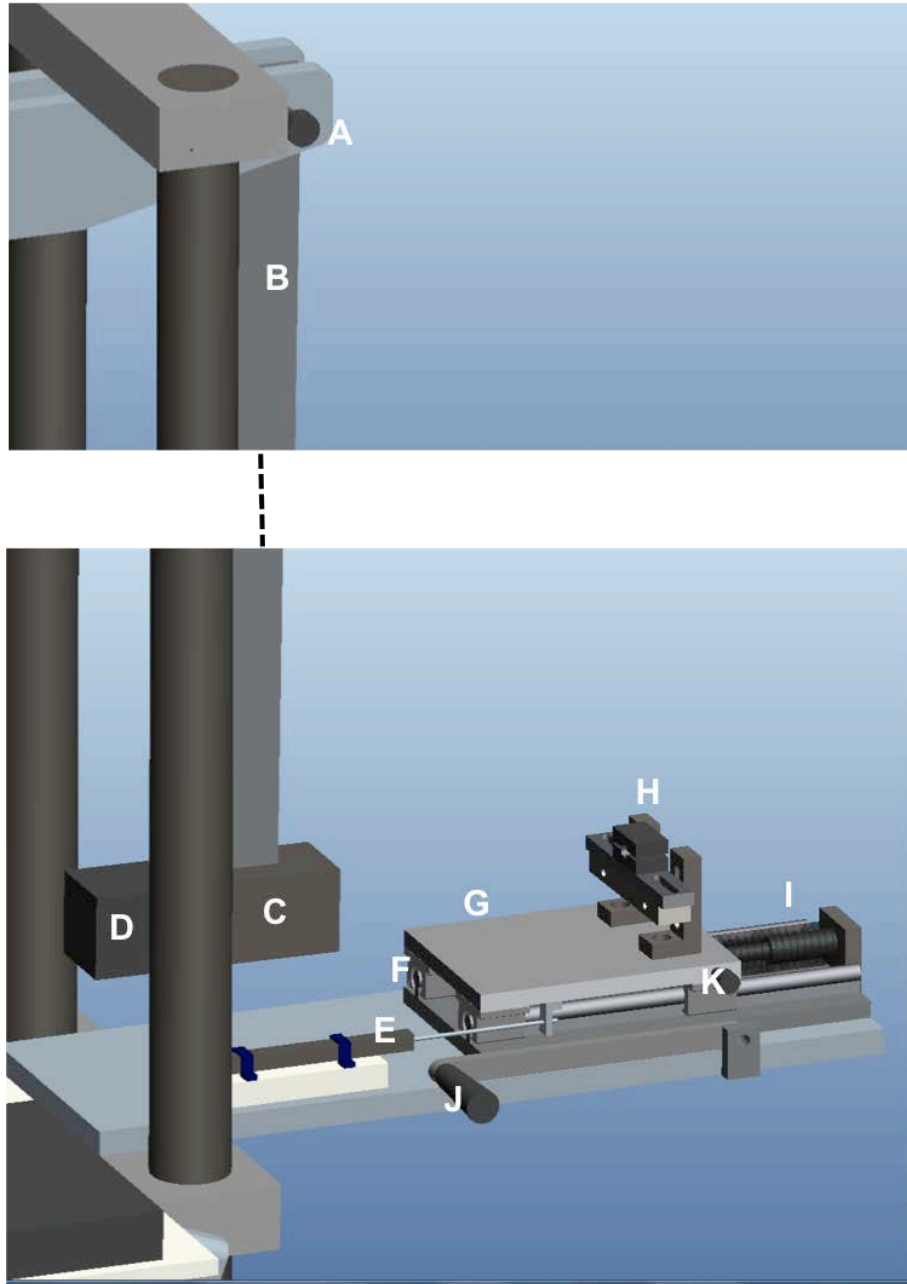
Figure 33: Close-up schematic of the finalized pendulum device. The locations of the rotary potentiometer (A), pendulum arm (B), original pendulum drop mass (C), additional pendulum drop mass attached (D), linear potentiometer (E), linear bearings (F), sled (G), adjustable mounting mechanism (H), coil spring (I), sled lever (J), and cam follower (K) are as noted.

### 3.3 Data Collection Technique

In order to collect the voltage data from the potentiometers, LabVIEW SignalExpress (National Instruments Corp., Austin, TX) was used. A referenced single ended (RSE) voltage setup with two analog voltage inputs (rotary potentiometer and linear potentiometer) was implemented with a digital trigger (foot trigger). Two seconds of potentiometer data were collected (30,000 samples at 15,000 hertz) for a single impaction. The average duration between the release of the pendulum drop mass and the end of an impaction was 0.7 seconds, so two seconds was sufficient time to gather the entire impaction history information. The sampling rate was chosen for enough samples to be collected to filter the signal and eliminate any unwanted noise. Once collected in LabVIEW, the raw voltage data were exported to Excel for permanent record.

With the raw voltage data saved in Excel, a custom MATLAB script was written to automate the process of converting the voltage information into the desired energy information. The script could analyze a single file or a folder of Excel files. To start, both potentiometer signals were filtered through an 11-point moving average filter to attenuate the high frequency noise components. The appropriate number of points to average was chosen by analyzing the preliminary impaction information. An 11-point moving average filter minimized the amount of memory required for computation, while effectively removing the high frequency noise signals. After filtering, the voltage history from the rotary potentiometer was converted into linear position history. The linear position history was plotted for graphical representation of the impaction, so that the user could identify any possible signs of error. The maximum slope (derivative) of the linear position prior to impact was found, and was used to calculate the pre-impact kinetic energy of the pendulum drop mass. Next, the linear potentiometer voltage information was converted into linear displacement information. With the known spring constant, the maximum linear displacement was used to calculate the post-impact sled energy. The difference between the calculated pre-impact kinetic energy and post-impact sled energy

was the energy absorbed by the specimen during impaction. The specimen number, pre-impact kinetic energy, post-impact sled energy, and energy absorption information were also automatically saved in an Excel format for permanent record and future user manipulation. Again, the entire process is automated using the custom MATLAB script, so meaningful results could be seen and saved in just a few seconds. With the final pendulum device and data collection technique established, the device and methodology were then ready for validation.

CHAPTER 4: VALIDATION STUDIES

This chapter discusses the studies that were conducted to validate the final version of the pendulum device and its associated methodology. Two major validation studies were conducted. The first validation study used foam specimens, which allowed for a more controllable impaction and additional measurement ability. The second validation study used foam and cadaver leg specimens, which was conducted to bridge between the foam specimen validation study and contemplated *in vivo* IAF experiments. The validation studies and corresponding results are outlined in the following sections.

4.1 Foam Specimen Validation Study

The foam specimen validation study used polyurethane foam (density of 240 kilograms per cubic meter) surrogates as stand-ins for the porcine hock specimens. To maintain a more controlled impaction, an aluminum specimen indenter was machined using a HAAS Precision Collet Lathe, to temporarily replace the tripod anchorage system. The specimen indenter would indent the foam during impaction, rather than causing fracture. This provided the ability to visualize and quantify the damage received by the specimen. The experimental methods and results of the foam specimen validation study were as follows.

4.1.1 Experimental Methods

Nine foam specimens were cut to size (2.5 x 3.8 x 3.8 centimeters) to conveniently fit on the specimen sled for impaction. The orientation of the indenter and foam specimens are shown in Figure 34. Each foam specimen could be impacted twice on the same face—once on the bottom and once on the top. Foam specimens were impacted six times at each of the three predetermined drop angles (20°, 40°, 60°). The previously described data collection technique was utilized to gather the pre-impact kinetic energy and post-impact sled energy information. As before, the energy absorption

was defined as the difference between the pre- and post-impact energies. After impaction, the foam's penetration depth caused by the indenter was measured with a digital caliper.
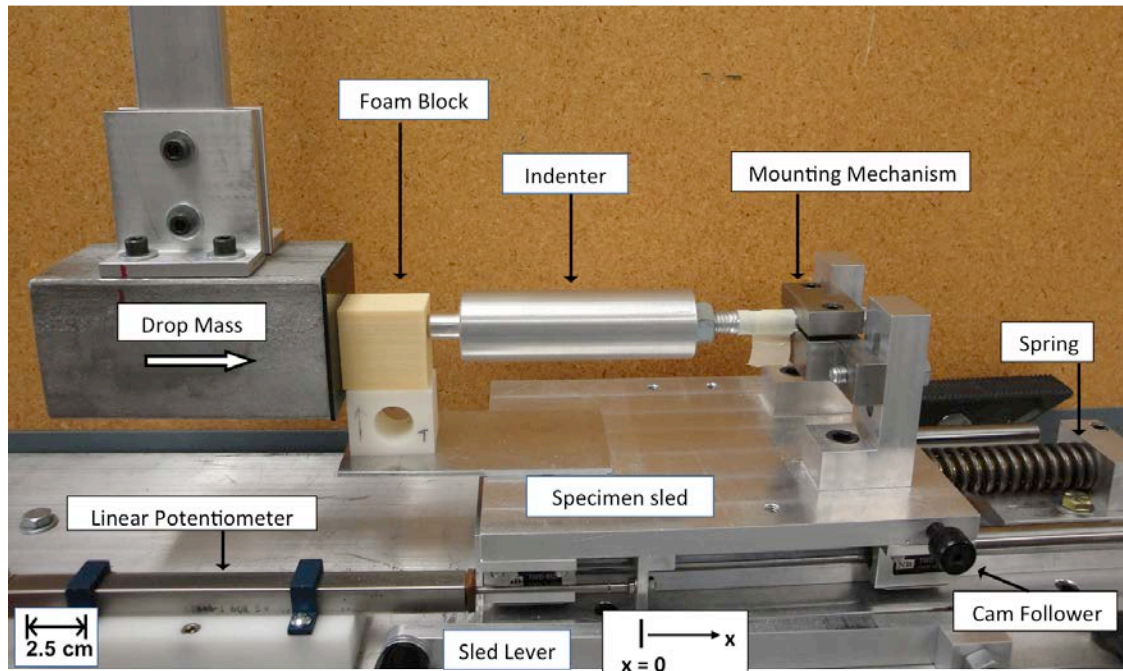


Figure 34: Pendulum device with indenter rigidly fixed with the mounting mechanism and foam specimen sitting on the low-friction sled.

Nine specimens of the same dimensions were also cut for indentation using an MTS 858 Bionix materials testing machine (MTS Systems Corp., Eden Prairie, MN). Again, each specimen was indented twice with the same indenter. The penetration depths measured from the first nine specimens were mimicked using the displacement control of the MTS, so the penetration depths between the first and second nine specimens would be similar. After indentation, penetration depths were again measured with a digital caliper. The force-displacement information was collected during the MTS indentations. The area under the force-displacement curve was calculated to find the energy absorbed by the

specimen. The energy absorption calculations between the potentiometer data and the MTS data were compared to investigate correlation.

### 4.1.2 Experiment Results

Both qualitative and quantitative experimental results from the foam specimen validation study are presented and discussed in this section. The qualitative penetration depth results of the foam specimens post-impact are illustrated in Figure 35. Penetration depth can be thought of as a more conceptual representation of energy absorbed by a foam specimen. It is logical to say that an increase in energy absorption would cause an increase in penetration depth. From basic visual observation, it is evident that a larger drop angle resulted in greater penetration depth, as was expected. The quantitative results (Figure 36), from the potentiometer and MTS data, show the extremely high correlation between the energy absorption calculations. The energy absorption calculation from the potentiometer data incorporates the energy absorbed by the entire system (i.e., indentation, friction, and the pendulum device itself). The energy absorption calculation from the MTS data only included the energy due to indentation of the specimen. Because of this difference, the energy absorption calculation from the potentiometer data was slightly greater than that from the MTS data. These results show that the technique surrounding the energy absorption calculation is indeed valid and accurately represents the amount of energy absorbed by a specimen during an impaction. However, does the foam specimen validation study really apply to the case of cadaver leg or *in vivo* porcine IAFs? To draw a connection between the foam specimen impactions and porcine IAF impactions, another validation study was carried out.
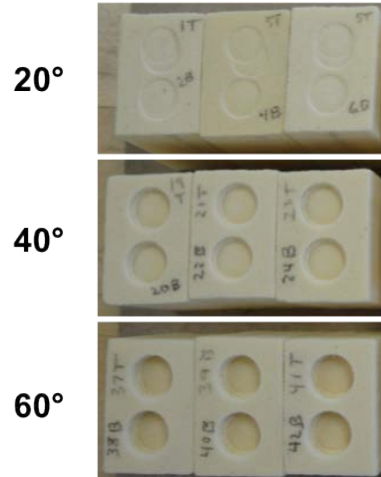
Figure 35: Post-impact foam specimens with visual indentations. Each specimen was impacted twice—once on the bottom and once on the top. The top six impactions were conducted at an initial drop angle of 20°, the middle six at 40°, and the bottom six at 60°. For some impactions at the low drop angle, two indentations were evident in a single impaction. At the higher drop angles, two indentations did not occur. The penetration depth clearly increased with an increase in drop angle.
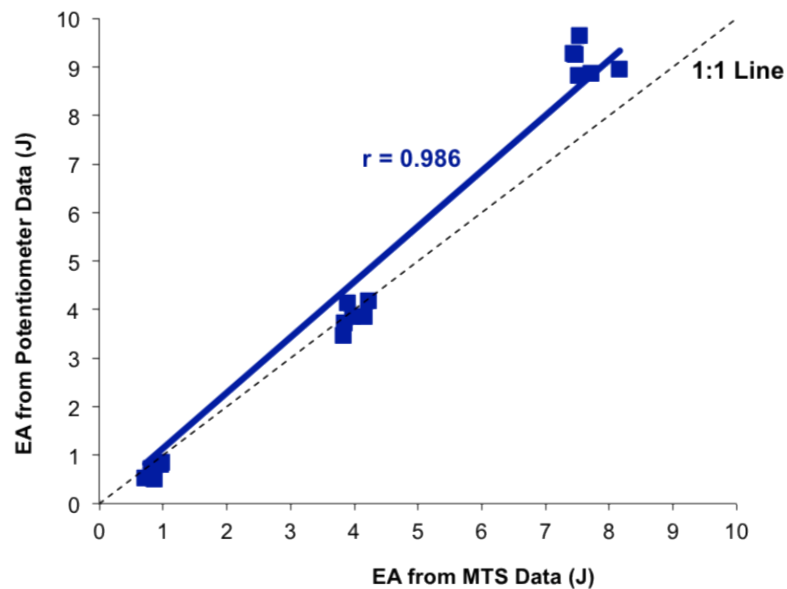


Figure 36: Relationship between energy absorption calculations from the potentiometer data and MTS data.

## 4.2 Motion Capture Validation Study

The motion capture validation study used two types of specimens: (i) polyurethane surrogates like those in the previous validation study, and (ii) cadaver leg porcine hock specimens. A motion capture system (Oqus Camera Series, Qualisys AB, Gothenburg, Sweden) was utilized to provide optical kinematic measurements and high-speed digital video of specimen impactions. This information was gathered to link the validity of the foam specimen impactions to those for cadaver leg (and *in vivo*) impactions. The experimental methods and results of the motion capture validation study were as follows.

### 4.2.1 Experimental Methods

Similar to the previous validation study, nine foam specimens were cut to size (2.5 x 3.8 x 3.8 centimeters) for impaction. Three foam specimens were impacted at each of the three predetermined drop angles (20°, 40°, 60°). In addition, the same methodology was used to gather the pre-impact kinetic energy, post-impact sled energy, energy absorption, and penetration depth measurements. Four motion capture cameras were positioned to track information from markers that were placed on the pendulum drop mass, foam specimen, and tripod anchorage system. The marker on the tripod anchorage system was equivalent to having one on the mounting mechanism, since they are rigidly fixed to each other. The advantage to having the marker on the tripod anchorage system instead of on the mounting mechanism was related to camera window size. With a smaller window size (i.e., a smaller field of view), more data could be captured at a higher sampling rate, which was desirable given the rapid nature of the impactions. The marker on the foam specimen was only used for visual assurance of the specimen's position, since the foam specimen was not rigidly fixed to the pendulum. A hand trigger was used to begin data collection, similar to the foot trigger for the pendulum device. Once the motion capture system was properly positioned and ready, foam specimen

impactions were conducted. Two seconds of potentiometer data, 3D position data, and high-speed digital video were all simultaneously collected via the previously discussed data collection technique and the motion capture system. A sampling rate of 4 kilohertz was chosen for the motion capture system, because that was the maximum possible rate for the selected window size.

In succession to the foam specimen impactions, five cadaver leg porcine hock specimens were impacted at a drop angle of 67°. This drop angle corresponded to an initial gravitational potential energy measurement of 35 joules, which was representative of preliminary IAF impactions *in vivo*. The motion capture device remained in position for the cadaver leg impactions. However, since a marker could not meaningfully be used if attached to the specimen, markers were only placed on the pendulum drop mass and tripod anchorage system. As in the foam specimen impactions, two seconds of potentiometer data, 3D position data, and high-speed digital video were all simultaneously collected for the cadaver leg impactions.

For both types of specimens, the potentiometer data were used to calculate the respective energy values, as was done in the foam specimen validation study. The 3D position data gave the position history of the pendulum drop mass and mounting mechanism. Once the 3D position data were exported to Excel, basic manipulation of the data was conducted to extract the desired information. From the pendulum drop mass position data, the linear velocity could be found to calculate the time history of the mass's kinetic energy. From the mounting mechanism position data and known spring constant, a time history of the sled energy could be calculated. From these two energy measurements, the energy absorption value could then be found. The energy measurements from the 3D position data were compared to the measurements from the potentiometer data. The initial length or distance between the pendulum drop mass and mounting mechanism markers was also found and defined as $L_i$. During the course of a foam impaction, the initial length would decrease as the indenter was penetrating the

specimen. The final length between the two markers was found and defined as $L_f$. The metric for the difference between initial and final lengths, $\Delta L$, was designated as the specimen deformation. Figure 37 illustrates the configuration of the four motion capture cameras, the associated markers, and the specimen deformation metric. In the foam impaction cases, it was assumed that the specimen deformation metric would closely resemble the penetration depth measurement. The relationship between these two was analyzed to confirm the aforementioned assumption. If the specimen deformation metric were equivalent to penetration depth in the foam impactions, then it could also be applied to the cadaver leg impactions for comparison. The high-speed digital video was also used to visually confirm the 3D position data and to provide an understanding of the specimen's motion history throughout impaction.
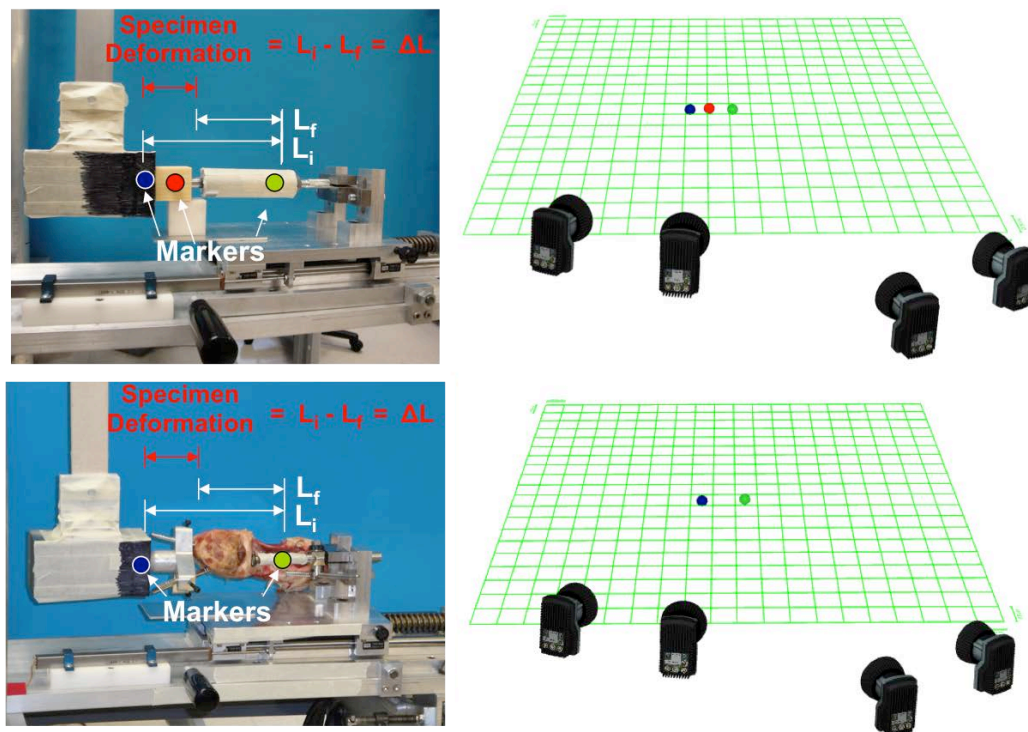


Figure 37:  Motion capture system setup for the foam surrogate specimens (top) and cadaver leg porcine hock specimens (bottom). The markers and specimen deformation metric are labeled.

4.2.2 Experiment Results

Comparison between the energy calculations from the 3D position data and potentiometer data can be seen in Table 2 for the foam impactions. It is evident that the energy calculations from the motion capture information are similar to the energy calculations from the potentiometer information. This confirms that the pendulum device instrumentation and data collection technique are accurate.

Table 2:    Energy measurement results from the potentiometer and motion capture data for each foam specimen, where KE is the kinetic energy, SE is sled energy, and EA is energy absorption.

| Specimen # | Drop Angle (°) | KE from Potentiometer Data (J) | KE from Motion Capture Data (J) | SE from Potentiometer Data (J) | SE from Motion Capture Data (J) | EA from Potentiometer Data (J) | EA from Motion Capture Data (J) |
|---|---|---|---|---|---|---|---|
| 1 | 20 | 2.3 | 2.2 | 1.6 | 1.6 | 0.7 | 0.6 |
| 2 | 20 | 2.2 | 2.0 | 1.4 | 1.3 | 0.8 | 0.7 |
| 3 | 20 | 2.1 | 1.8 | 1.2 | 1.1 | 0.9 | 0.7 |
| 4 | 40 | 8.7 | 8.5 | 5.1 | 5.2 | 3.6 | 3.3 |
| 5 | 40 | 8.9 | 8.8 | 4.6 | 5.1 | 4.3 | 3.7 |
| 6 | 40 | 9.0 | 8.8 | 4.9 | 4.7 | 4.1 | 4.1 |
| 7 | 60 | 19.4 | 19.0 | 10.4 | 11.1 | 9.0 | 7.9 |
| 8 | 60 | 19.3 | 18.9 | 8.9 | 9.7 | 10.4 | 9.2 |
| 9 | 60 | 19.1 | 18.9 | 8.3 | 9.0 | 10.8 | 9.9 |

Visual observations of the foam specimens post-impact were also consistent with the qualitative penetration depth results seen in the foam specimen validation study. The comparison between the penetration depth and specimen deformation measurements for each of the three drop angles can be seen in Table 3. It is evident that the specimen deformation and penetration depth measurements are indeed approximately equivalent. Therefore, the specimen deformation measurement meaningfully applied to the cadaver leg impactions.

Table 3:    Foam specimen penetration depth and specimen deformation measurements.

| Specimen # | Drop Angle (°) | Penetration Depth (mm) | Specimen Deformation (mm) |
|---|---|---|---|
| 1 | 20 | 0.45 | 0.58 |
| 2 | 20 | 0.50 | 0.77 |
| 3 | 20 | 0.60 | 0.77 |
| 4 | 40 | 2.35 | 2.45 |
| 5 | 40 | 3.10 | 3.30 |
| 6 | 40 | 3.50 | 3.61 |
| 7 | 60 | 4.80 | 4.69 |
| 8 | 60 | 5.70 | 5.93 |
| 9 | 60 | 6.75 | 7.09 |

From the motion capture information, the energy and specimen deformation histories for a representative foam impaction are shown in Figure 38. It can be seen that the majority of the pre-impact kinetic energy was transferred to the specimen and sled early during the impaction event. The kinetic energy was not entirely transferred to the specimen and sled until the sled's forward motion was halted and reached its maximum displacement. The sled energy gradually increased from the initial time of impaction until the sled's forward motion was halted upon reaching its maximum displacement. The specimen deformation history revealed the interesting kinematic behavior of the foam specimen during an impaction. The majority of the specimen deformation occurred during the beginning of impaction. Near the instant of the sled's maximum displacement, the maximum specimen deformation was also reached. The double-peak feature of the specimen deformation curve was explained from the high-speed digital video. The foam specimen was being penetrated during the initial peak, while the low-friction sled was still beginning to accelerate forward. After the first peak, the sled began to move slightly

faster than the pendulum drop mass. Due to the measurement technique of the specimen deformation metric, a decrease in specimen deformation was seen on the history curve. With the coil spring constantly resisting the sled's forward motion, the pendulum drop mass started to reconnect with the foam specimen. This was the cause of the second peak, where the maximum specimen deformation occurred. Shortly there after, the sled's forward motion was halted by the coil spring. The high-speed digital video confirmed the characteristics of the energy and specimen deformation histories in the foam specimen impactions. Again, it is important to note that the majority of the penetration depth occurred during the beginning of impaction, which the first specimen deformation peak alluded to.
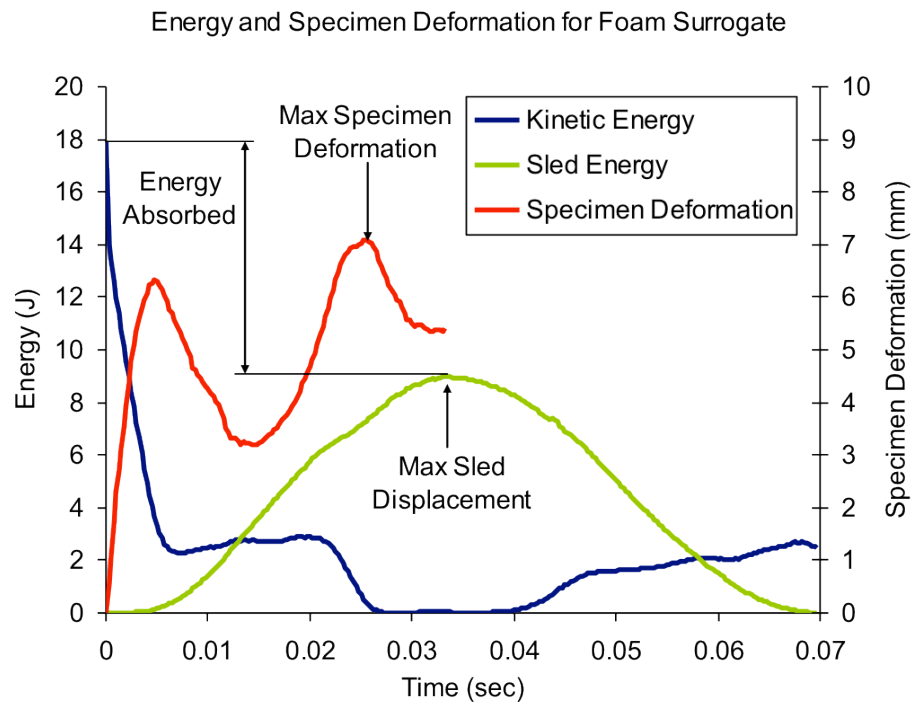


Figure 38: Kinetic energy, sled energy, and specimen deformation histories for a representative foam impaction.

For the cadaver leg specimen impactions, the energy and specimen deformation histories of a representative impaction are shown in Figure 39. The cadaver leg impaction results were strikingly similar to the foam impaction results. The majority of the pre-impact kinetic energy was again transferred to the specimen and sled during the beginning of impaction. The sled energy again gradually increased from the initial time of impaction until the sled's forward motion was halted. The majority of the specimen deformation again occurred during the beginning of impaction. However, the double-peak was not as dramatic for the foam impaction. Following the first specimen deformation peak, the deformation curve gradually increased until the sled's forward motion was halted by the coil spring. The high-speed digital video also confirmed the characteristics of the energy and specimen deformation histories in the cadaver leg specimen impactions. From the video information, it also appeared that the initial IAF of the cadaver leg specimen was created during the beginning of impaction.

The motion capture results from the foam and cadaver leg impactions revealed many similarities. The energy history information was nearly identical, and the specimen deformation histories were also very comparable. In addition, both the foam and cadaver leg specimens experienced the majority of their damage during the initial portions of impaction. Based on the similarities seen in the motion capture validation study, the energy absorption measurement technique that was validated in the foam specimen validation study could indeed be reasonably applied to cadaver leg and *in vivo* impactions. With the energy absorption measurement technique successfully validated, *in vivo* impactions could finally be conducted. The materials and methods for the *in vivo* fracture specimens are set forth in the next chapter.
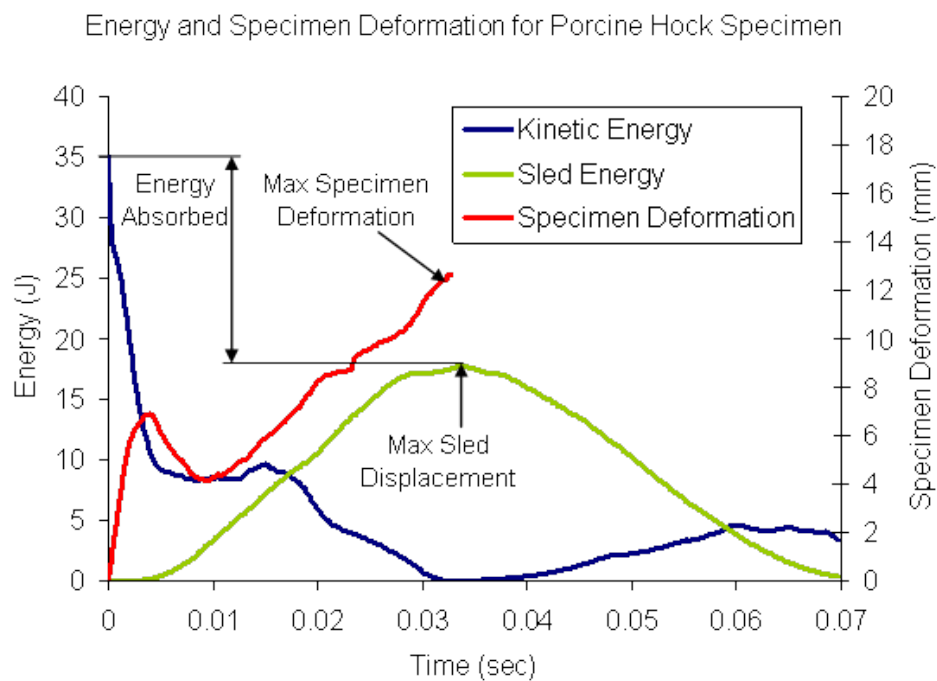
Figure 39: Kinetic energy, sled energy, and specimen deformation histories for a
representative cadaver leg porcine hock impaction.

CHAPTER 5: MATERIALS AND METHODS FOR *IN*

*VIVO* FRACTURE ANIMALS

This chapter outlines the materials and methods that were used for *in vivo* porcine IAF creation, work still ongoing at the time of this writing. The steps taken in preparing for the live animal impaction are discussed, as well as the surgical procedure for attaching the tripod anchorage system, the impaction technique for IAF creation, and the post-impact surgical and animal care procedures.

Eleven Yucatan miniature pigs (IACUC-approved, ACURF #1007141) have been impacted to date using the pendulum device and data collection technique. Animals #1-4 were impacted in the spring of 2011. Animals #5-11 were impacted in the spring of 2012. For the remainder of the materials and methods, focus will be placed on those animals that have already been impacted. Future plans with the ongoing *in vivo* study will be discussed in Chapter 6.

## 5.1 Preparation for the Live Animal Impaction

The first four Yucatan miniature pigs (age of approximately two years and weight of 55 kilograms) were obtained from Sinclair Bio Resources (Auxvasse, MO). The next seven Yucatan miniature pigs (age of approximately two years and weight of 90 kilograms) were obtained from Exemplar Genetics (Sioux Center, IA). The animals were maintained according to University of Iowa animal care guidelines. Experimental surgeries were performed by an experienced orthopaedic surgeon, while using inhalation anesthesia and aseptic technique.

Before the surgical procedure commenced, appropriate steps were conducted to ensure the pendulum device and data collection hardware were operating correctly. The voltages from the power supplies were checked to confirm that they were supplying each of the potentiometers with 10 volts. With the correct voltage being supplied, the voltages from the resting positions of each potentiometer were recorded. These voltages were

checked with previous records, as they were also needed for the energy calculations. The sled lever was used to test the linear potentiometer by moving the low-friction sled. Similarly, the pendulum arm was rotated to test the rotary potentiometer. The foot trigger was also tested multiple times to ensure the batteries were still supplying 3 volts when triggered.

## 5.2 Pre-Impact Surgical Procedure

After the animal was prepared and the hardware tested, the orthopaedic surgeon performed surgery to attach the tripod anchorage system to the hock joint. The surgical procedure was similar to that discussed above for the tripod anchorage system section—attention is directed to Figure 11 for reference. The three external fixator pins (6 millimeter diameter, Orthofix Inc., Lewisville, Texas) were used to fix the aluminum impact interface to the talus. Two external fixator pins were directly inserted into the talus, inferomedially. The third external fixator pin was inserted through the talocalcaneal joint into the talus. The inserted external fixator pins effectively created a tripod configuration, hence the nomenclature of the anchorage system. Next, the leg holder device was attached to the tibia. The distal tibia plate was attached using two plugs and a cortical screw, which were inserted into the anterior distal tibial surface. The plate's ball-and-socket joint allowed the leg holder shaft to be properly oriented for impaction. The leg holder shaft gripped another external fixator pin that was inserted through the proximal tibia. This attachment had the dual purpose of maintaining the inclination of the tibial shaft (approximately 45°) and maintaining the orientation of the leg holder shaft in the direction of impact mass travel. After the tripod anchorage system was successfully attached to the joint, the stress-rising saw cut was created using an oscillating bone saw (Stryker Corp., Kalamazoo, MI) to ensure a consistent fracture pattern.

## 5.3 Intraarticular Fracture Creation

Once the tripod anchorage system was attached properly to the animal, the pendulum device and data collection technique were used to create the IAF insult. The surgical utensil tables and fluoroscopy equipment were removed from the immediate surgical field, while the pendulum device and data collection hardware were introduced. The specimen table was placed over the operating table and under the specimen joint. The leg holder shaft of the tripod anchorage system was positioned into the mounting mechanism and adjusted until the impact interface was centered about the pendulum drop mass. Once the tripod anchorage system and animal joint were properly positioned, the mounting mechanism bolts were tightened to lock the leg holder shaft in place. Figure 40 shows the pendulum device in the surgical environment with the animal leg properly mounted prior to fracture. The data collection software was commanded to collect two seconds of potentiometer voltage data when triggered. The pendulum drop mass was raised to the desired drop angle by observing the panel meter information. The foot trigger was pressed, and the pendulum drop mass was released from the correct angle. The pendulum drop mass was then manually caught following impaction, so as to prevent a second impaction. After impaction, the orthopaedic surgeon observed the damage to the animal (Figure 41). If it was determined that the initial IAF attempt was not successful, another impaction was performed. Often, in the case of another impaction, the drop angle was increased to improve the chances for IAF occurrence. The potentiometer data from each impaction were recorded in LabVIEW and exported to Excel. To reiterate, the voltage output from the rotary potentiometer corresponded to the angular position of the pendulum arm. From the angular position information, the linear velocity could be found and used to calculate the kinetic energy of the pendulum drop mass immediately before impact (pre-impact kinetic energy). The voltage output from the linear potentiometer corresponded to the linear position of the low-friction sled. From the linear position information and the known spring constant, the energy required for the coil spring to stop

the low-friction sled's forward progress (post-impact sled energy) could be calculated. The energy absorption measurement was then the difference between the pre-impact kinetic energy and post-impact sled energy. As previously discussed, a custom MATLAB script automatically analyzed the data and calculated the kinetic energy, sled energy, and energy absorption measurements. Again, the final information was exported to Excel for permanent record. Following a successful fracture insult, the pendulum device and data collection hardware were removed from the immediate surgical field, and then the surgical utensil tables and fluoroscopy equipment were reintroduced.
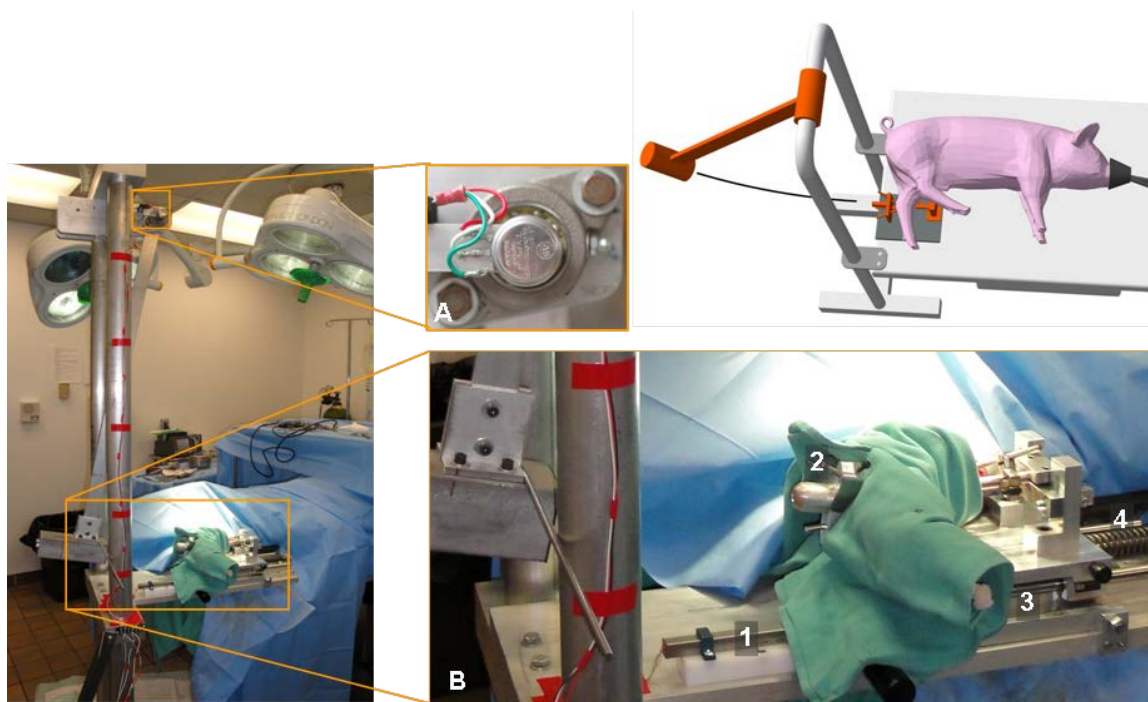


Figure 40:  Pendulum device *in vivo*, including a rotary potentiometer that measured the pendulum's linear velocity (A), the linear potentiometer that measured the sled's linear displacement (B1), the specimen anchorage system (B2), the low-friction sled on linear bearings (B3), and the coil spring that resisted the sled's forward motion (B4).

Figure 41: Orthopaedic surgeon checking for post-impact fracture.

## 5.4 Post-Impact Surgical Procedure and Animal Care

Immediately following the fracture insult, the orthopaedic surgeon prepared to anatomically reduce the fracture fragments. A 2.1-millimeter thick tibial plateau leveling osteotomy (TPLO) plate, specifically designed for veterinary surgery (Synthes Vet, West Chester, PA), was surgically fixed across the distal tibial fracture with six 2.7-millimeter bone screws. Once the TPLO plate was in place (Figure 42), the open incisions were sutured closed. Following suture, the animal joint was put in a surgical cast for a week, and the animals were again maintained according to University of Iowa animal care guidelines. In addition to the radiographs taken before fracture insult (baseline) and immediately after fracture, radiographs were also taken after anatomical reduction and at various time points post-fracture (1, 2, 4, 8, and 12 weeks). Mainly, the radiographs allowed the orthopaedic surgeon to identify the characteristics of each fracture and observe the corresponding bone healing progression.
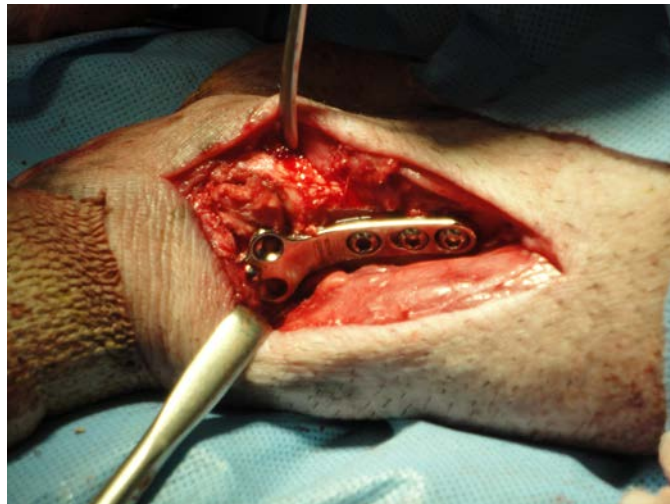
Figure 42:  Tibial plateau leveling osteotomy plate across the post-impact IAF insult.

CHAPTER 6: RESULTS & DISCUSSION

This chapter presents the results from the eleven animals studied to date, including IAF creation and energy measurement results. The animals were divided into two groups based on the date of impactions and the associated experimental variables.

### 6.1 Live Animals #1-4

#### 6.1.1 Intraarticular Fracture Creation Results & Discussion

Being the first *in vivo* impaction that was conducted, Animal #1 not unexpectedly experienced some complications. The first attempt at fracturing the joint was not successful using a drop angle that corresponded to 20 joules of initial gravitational potential energy. Two additional attempts at a 30-joule impact and a fourth attempt at 40 joules were needed to finally produce fracture. The need for multiple impactions could possibly be explained due to inexperience. Mainly, the necessary drop angle to produce a sufficient magnitude of pre-impact energy to cause fracture was not known. From the four fracture attempts in Animal #1, clearly an initial gravitational potential energy greater than 30 joules would be required in the porcine animals to follow. To account for a larger energy magnitude, the coil spring (spring #2 discussed in Chapter 2) was upgraded to a spring that possessed a larger energy capacity (spring #3). The pendulum drop mass that was used for Animal #1 allowed for a maximum initial gravitational potential energy of only 38 joules at 90° (maximum angle for consistent manual release). Any needed increase in pre-impact energy would not be possible, so the pendulum drop mass was increased. It should also be noted that the severity of fracture following the fourth fracture attempt was greater than what was preferred. This could have been related to the multiple impactions that were delivered to the animal joint. The one-day post-surgical reduction radiograph showing the fracture and TPLO plate from Animal #1 can be seen in Figure 43.

Figure 43: One-day post-fracture radiograph of the fracture insult and TPLO plate from Animal #1.

After the pendulum system upgrades were completed, Animals #2-4 were impacted. Animals #2 and #3 did not experience the same complications as Animal #1. Both animals successfully fractured with a single impaction with an initial gravitational potential energy of 33 joules. This was much more encouraging than Animal #1. From these results, it appeared that the additional mass and spring #3 were sufficient for fracture creation. When Animal #4 was impacted under the same conditions as Animals #2 and #3, however, fracture did not occur after a first impaction with an initial gravitational potential energy of 33 joules. After a second impaction at 40 joules, however, fracture was successfully created. The post-surgical reduction radiographs from Animals #2-4 were similar to the radiograph from the first animal. The severities of the IAFs created in Animals #2-4 were less than the IAF created in Animal #1. Moreover, the IAFs created in Animals #2-4 were morpholically consistent with human ankle fractures, which was a central objective for the *in vivo* study.

6.1.2 Energy Measurement Results & Discussion

The experience with data collection and the energy measurement results for the first four animals are discussed in this section. The associated variables and energy measurement results for these animals are shown in Table 4.

Table 4:    Energy measurement results for Animals #1-4.

| Animal # | Impact # | Drop Mass (kg) | Spring # | Stopping Mechanism Y/N | Theoretical Potential Energy (J) | Kinetic Energy (J) | Sled Energy (J) | Energy Absorbed (J) |
|---|---|---|---|---|---|---|---|---|
| 1 | 4 | 3.88 | 2 | Y | 40 | 45 | 14 | 32 |
| 2 | 1 | 5.82 | 3 | Y | 33 | 24 | 12 | 12 |
| 3 | 1 | 5.82 | 3 | Y | 33 | 26 | 11 | 14 |
| 4 | 2 | 5.82 | 3 | Y | 40 | 32 | 15 | 17 |

Note:  The associated variables are given, such as pendulum drop mass, spring number, whether or not the stopping mechanism was used, and the theoretical gravitational potential energy of impaction.

For Animal #1, the energy absorption measurement was 32 joules during the final impact, for which fracture occurred. It was apparent from the spring energy measurement that the maximum energy capacity of spring #2 was being reached. Therefore, the energy absorption that was calculated could have been greater than the energy actually absorbed physically. When comparing the kinetic energy value to the theoretical potential energy value, the kinetic energy was greater, which was not expected. This could be explained by analyzing the voltage outputs from the potentiometers (Figure 44). The initial reading of the rotary potentiometer indicated that the sliding contact reached its zero voltage position at such a high drop angle (>100°). Therefore, the theoretical potential energy value was not as high as it should have been, causing it to be less than the kinetic energy value. These energy measurement results confirmed the initial need for upgrades based on the IAF creation results. The additional mass would eliminate the need for excessive

drop angles, thus allowing for more accurate energy measurements and for a more user-friendly release of the pendulum drop mass. The upgraded spring would also allow for the needed increase in energy capacity.



Figure 44:  Linear and rotary potentiometer voltage outputs for Animal #1. The linear displacement graph shows the sled beginning to translate at around 0.9 seconds (when impaction initiated). The displacement remained at 4.4 centimeters because the stopping mechanism was used.

To reiterate, Animals #2-4 were impacted after the additional mass and spring #3 were attached. Animals #2 and #3 had energy absorption measurements of 12 and 14 joules, respectively. The voltage outputs from the potentiometers did not experience the

same problem as in Animal #1 (Figure 45). For Animal #4, the energy absorption measurement was 17 joules during the impact that induced fracture. It appeared that the additional mass and updated spring were sufficient for the *in vivo* impactions, but other improvements needed to be made before proceeding to fracture more animals in subsequent *in vivo* impactions.



Figure 45: Linear and rotary potentiometer voltage outputs for Animal #2. The linear displacement graph shows the sled beginning to translate at around 0.8 seconds (when impaction initiated). The displacement remained at 3.3 centimeters because the stopping mechanism was used. These voltage outputs were similar to those from Animals #3 and #4.

### 6.1.3 Further Modifications

After observing the results and surgical procedure, further modifications were made to facilitate more fluid system operation. To start, the stopping mechanism experienced numerous problems, as discussed in Chapter 2. Consequently, it was decided to remove the stopping mechanism to eliminate those complications. The data collection hardware was upgraded and fixed to the pendulum, eliminating the need for extra cords and the data collection cart (see Chapter 2 for details). The adjustable mounting mechanism was also modified to allow for increased adjustability in the vertical and transverse directions (see Chapter 2 for details). These modifications made the pendulum device easier to operate, and allowed for increased animal maneuverability for the orthopaedic surgeon. Once the modifications were established, future *in vivo* impactions were conducted for an additional seven animals.

### 6.2 Live Animals #5-11

### 6.2.1 Intraarticular Fracture Creation Results & Discussion

Animals #5-11 were impacted after the modifications were implemented. Animals #5 and #6 required single impactions with an initial gravitational potential energy of 45 and 46 joules, respectively, to create a successful fracture. Fracture for Animal #7 required two impactions at 41 joules of initial gravitational potential energy. Animals #8 and #9 only required single impactions at 46 and 41 joules, respectively. For Animal #9, the initial gravitational potential energy was intended to be 45 joules. However, the drop angle of the pendulum arm was incorrect, due to user error in the release. Animal #10 needed to be impacted twice, at 45 and 46 joules, to achieve fracture. Following the first impaction, the orthopaedic surgeon re-adjusted the tripod anchorage system, because it was not properly aligned in the pendulum device. This was believed to be the cause of the first failed impaction. Therefore, the energy delivery magnitude was not deliberately increased for the second impaction. Animal #11 exhibited a successful fracture following

a single impaction of 46 joules. The post-surgical reduction radiographs for Animals #5-11 were similar to those of Animals #1-4. Similar to Animals #2-4, the IAFs created in Animals #5-11 were morphologically similar to human ankle fractures.

### 6.2.2 Energy Measurement Results & Discussion

The data collection technique and energy measurement results for Animals #5-11 are discussed in this section. The associated variables and energy measurement results for Animals #5-11 can be seen in Table 5.

Table 5:    Energy measurement results for Animals #5-11.

| Animal # | Impact # | Drop Mass (kg) | Spring # | Stopping Mechanism Y/N | Theoretical Potential Energy (J) | Kinetic Energy (J) | Sled Energy (J) | Energy Absorbed (J) |
|---|---|---|---|---|---|---|---|---|
| 5 | 1 | 5.82 | 3 | N | 45 | 44 | 15 | 28 |
| 6 | 1 | 5.82 | 4 | N | 46 | 41 | 20 | 21 |
| 7 | 2 | 5.82 | 4 | N | 41 | 38 | 18 | 20 |
| 8 | 1 | 5.82 | 4 | N | 46 | 41 | 20 | 21 |
| 9 | 1 | 5.82 | 4 | N | 41 | 38 | 18 | 20 |
| 10 | 2 | 5.82 | 4 | N | 46 | 42 | 19 | 23 |
| 11 | 1 | 5.82 | 4 | N | 46 | 41 | 21 | 20 |

Note:  The associated variables are given, such as pendulum drop mass, spring number, whether or not the stopping mechanism was used, and the theoretical gravitational potential energy of impaction.

For Animal #5, the energy absorption measurement was 28 joules during the final impact that induced fracture. When observing the spring energy measurement, the maximum energy capacity was being approached. The energy absorption measurement increased more than the input kinetic energy when compared to the results from Animal #4. The spring energy capacity being approached could have been the explanation for the higher energy absorption measurement. Therefore, it was decided to make a final spring

upgrade (spring #4) that would eliminate any possibility of reaching the maximum energy capacity.

After the final spring upgrade, Animals #6-11 were impacted. Typical voltage outputs from the potentiometers can be seen in Figure 46.
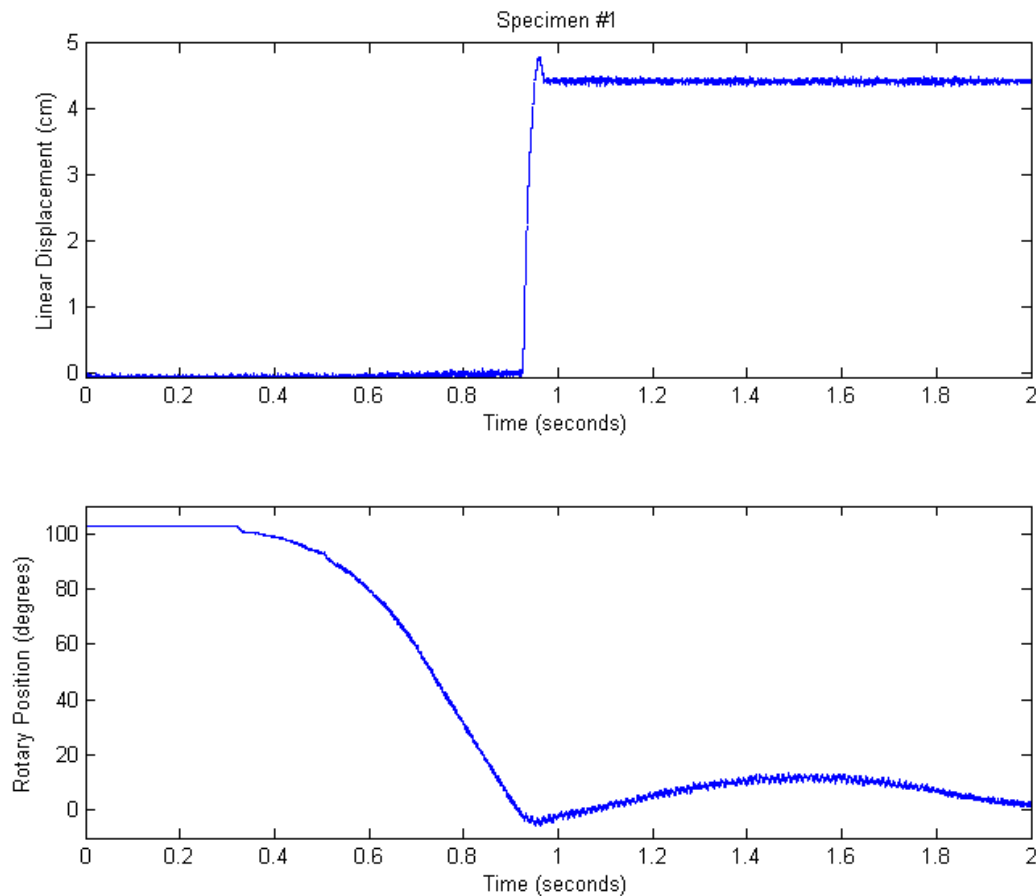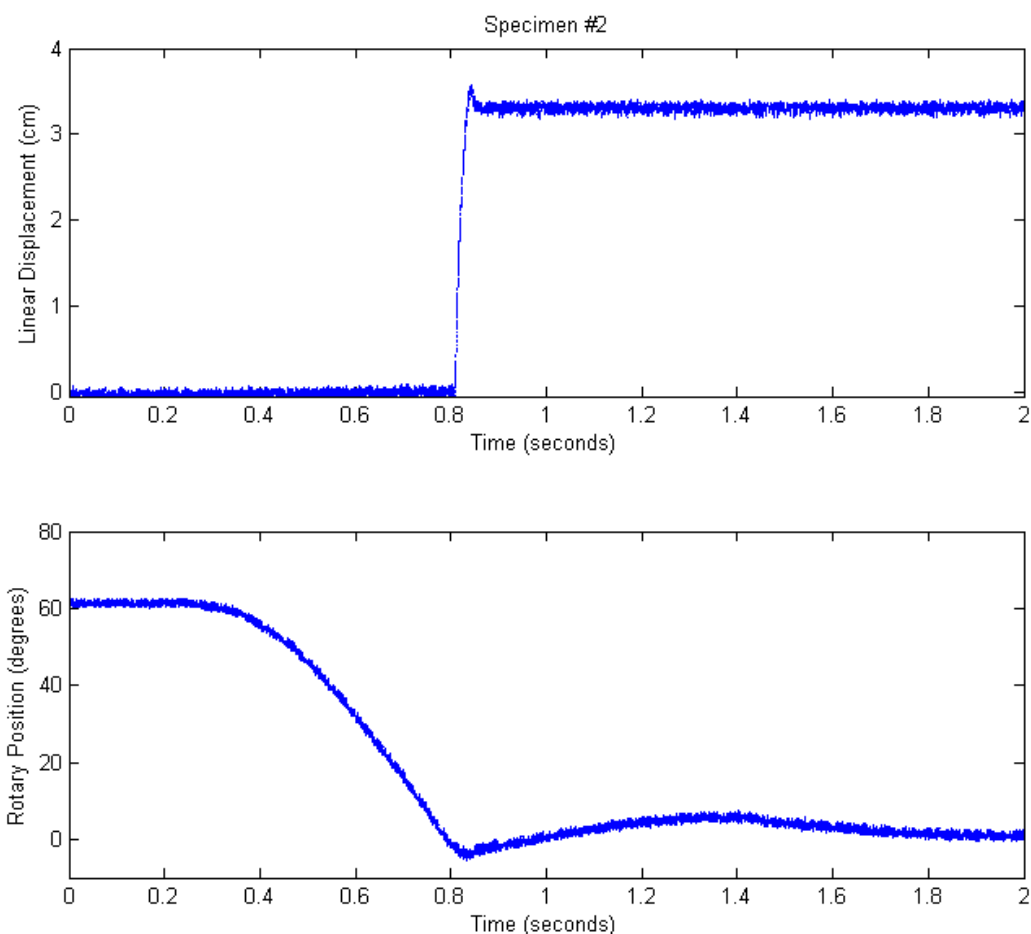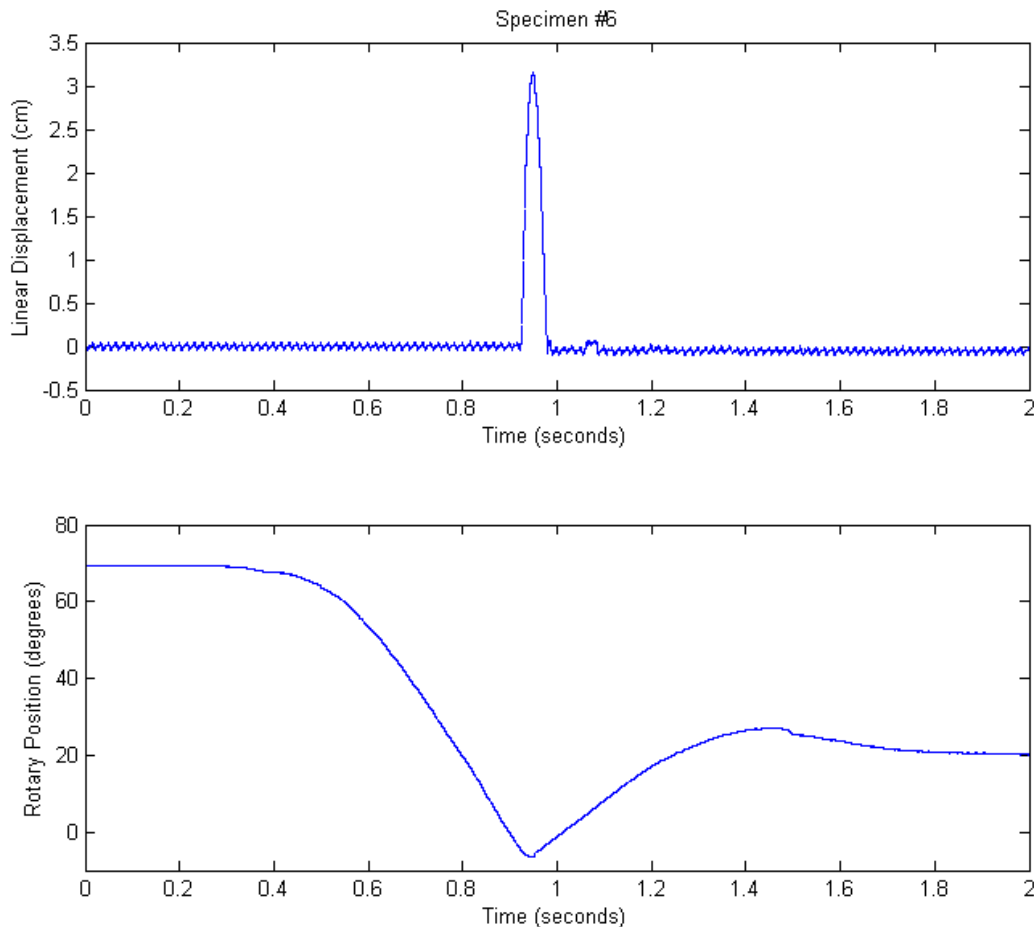


Figure 46:  Linear and rotary potentiometer voltage outputs for Animal #6. The linear displacement graph shows the sled beginning to translate at around 0.9 seconds (when impaction initiated). The stopping mechanism was not used, so the linear displacement returned to zero. These voltage outputs were similar to those from Animals #7-11.

Animal #6 had an energy absorption measurement of 21 joules. For Animal #7, the energy absorption measurement was 20 joules during the final impact that induced fracture. Animals #8 and #9 had energy absorption measurements of 21 and 20 joules, respectively. After the final impact, Animal #10 had an energy absorption measurement of 23 joules. For Animal #11, the energy absorption measurement was 20 joules.

### 6.3 Limitations and Potential Solutions

Despite the success of the pendulum device and data collection technique, there are some limitations that need to be addressed. First, the energy absorption measurement does not exclusively measure the fracture energy. Since the potentiometer data only provides the pre- and post-impact energies, the energy absorption measurement also includes energy that dissipates throughout the impaction to various avenues, including soft tissue deformation, friction, and the pendulum device itself. Further investigation of the motion capture data, should provide more information about the energy dissipation in real-time. This would allow for a better understanding of energy that solely corresponds to the fracture energy.

The user error in the release of the pendulum drop mass is another limitation of the pendulum device. A potential solution that would eliminate this source of error is a release mechanism. The release mechanism would ensure that the drop height of the pendulum drop mass was consistent between animals.

CHAPTER 7: CONCLUSION

This chapter discusses conclusions that can be drawn from the IAF creation and energy absorption measurement results of the first eleven animals that have been impacted to date in the *in vivo* porcine IAF study. In addition, future (funded) research that intends to use the described pendulum device and data collection technique will also be discussed. Finally, implications of this work are discussed applicable to the broader scope of other impaction devices that might be utilized in the future.

## 7.1 Intraarticular Fracture Creation

Looking at the success rate of IAF creation in the eleven animals impacted to date, fracture was successfully achieved in every instance. However, it was desirable for only a single impaction to be required to create fracture, which occurred in seven out of the eleven animals (64%). This success rate is low, but most of the failure instances were due to the learning process of developing such a novel IAF model. Animal #1 and #4 required multiple impactions because the magnitude of the initial gravitational potential energy needed to create fracture was not known. For the final six animals, the variables remained constant, except for the initial gravitational potential energy of Animal #7. Animal #7 was the only animal to intentionally receive an initial gravitational potential energy less than 45 joules, which resulted in the need for another impaction to create fracture. Animal #10 was the other animal that required a second impaction. Again, this apparently was due to surgical error in positioning the animal, which seemingly could be avoided in future impactions. If Animal #10 is disregarded due to this surgical error, the success rate for the other five animals was 80%. With additional practice and experience, minor inaccuracies like the surgical error in Animal #10 could potentially be avoided, leading the success rate of the IAF model to further improve. The current pendulum device and its modifications proved to be effective for creating fracture. Therefore, the desirable variables that would likely result in consistent fracture after a single impaction

in the future are: 5.82-kilogram drop mass, fourth spring, no stopping mechanism, and a drop angle corresponding to 45 joules of initial gravitational potential energy.

## 7.2 Energy Absorption Measurement

The energy absorption measurement results for the fractures in the first eleven animals exhibited some variability. The range of energy absorption measurements during fracture of the eleven animals was 11.7-31.8 joules, with a mean and standard deviation of $20.8 \pm 5.7$ joules. Both the range and the variance are quite large. However, if the animals are stratified based on the impaction variables, the sources of variability can be revealed. During fracture, the first five animals had an energy absorption measurement ranging from 11.7-31.8 joules, with a mean and standard deviation of $20.6 \pm 8.9$ joules. For the fractures in Animals #6-11, the energy absorption measurements ranged from 19.7-22.6 joules, with a mean and standard deviation of $20.9 \pm 1.1$ joules. From this information, it is evident that the large range and variability among the eleven animals resulted from experience in the first five animals. The variability in the first five animals could be explained by the variables that were being adjusted between animals to improve the consistency of fracture creation. After appropriate values of these variables were identified, Animals #6-11 demonstrated gratifyingly consistent energy absorption behavior. The consistency seen in Animals #6-11 further indicates that the data collection technique and energy absorption measurement are appropriate for the *in vivo* IAF model.

In addition to the consistency of Animals #6-11, the magnitude of energy absorption measurements was also in the range that is expected. On average, the energy absorption measurements were approximately 52% of the pre-impact kinetic energy values. This agreed with the values seen in the motion capture validation study, which had energy absorption measurements that were approximately 50 and 51% of the pre-impact kinetic energy values for the foam and cadaver leg porcine hock animals, respectively. The magnitude of energy absorption measurements for Animals #6-11 also

agreed with the work from Abdel-Wahab et al. [49], which showed that the energy absorption of cortical bone fracture in a controlled Izod impact test was approximately 51%. Based on these results, the magnitude of energy absorption measurements seems to be quite accurate for *in vivo* IAF work.

## 7.3 Future (Funded) Research

The ongoing *in vivo* porcine IAF study plans to impact another six animals in the next month. The current pendulum device and data collection technique will be used to collect the energy absorption measurements for these animals, as was done previously. Funding sources have committed support for a total of 48 animals to be impacted by the end of next year as part of the ongoing *in vivo* porcine IAF study. Once that study has been completed, an effective large animal IAF model will be established. The progression of chondrocyte damage associated with the established IAF model will allow for the testing of possible biological adjunct therapies for posttraumatic OA treatment. Once effective posttraumatic OA treatments are explored, they could possibly also be applied to treat other manifestations of OA.

## 7.4 Future of the Energy Absorption Technique

The current pendulum device and data collection technique are not limited to IAF insult in porcine animals. The described methodology could easily be applied to other large animals. Furthermore, its use could be applied to other impaction experiments, such as blunt impaction experiments, with a few minor adjustments to the physical pendulum device.

The idea of performing energy absorption measurement should also be considered and applied to other blunt impaction and fracture insult devices. As discussed in Chapter 1, most of the published blunt impaction and fracture insult devices can only calculate the initial gravitational potential energy of impaction. If future blunt impaction and fracture insult devices could incorporate energy absorption measurements, the actual amount of

energy damaging the animal could be controlled for. This would provide novel information associated with the pathomechanics of the induced injury.

In conclusion, the described pendulum device and data collection technique have been validated and effectively utilized in an ongoing *in vivo* porcine IAF study. The IAF creation results showed that the device was successful in creating fractures, while the energy absorption measurement results showed that the data collection technique was successful in quantifying the fracture insult. The methodology of this work is being applied to future animals in the ongoing *in vivo* porcine IAF research and seemingly can be implemented in future blunt impaction and fracture insult devices.

APPENDIX

Table A1: Dates and types of impaction tests that were conducted with the pendulum device.

| Date | Specimen Type | Number of Specimens | Linear Potentiometer # | Rotary Potentiometer # | Drop Mass (kg) | Spring # | Sled # | Indenter or Mount # | Stopping Mechanism Y/N | Notes |
|---|---|---|---|---|---|---|---|---|---|---|
| 12/20/10 | None | 35 | 1 | 1 | 3.88 | 1 | 1 | Indenter | Y | Initial testing |
| 01/27/11 | Foam | 14 | 2 | 1 | 5.82 | 1 | 1 | Indenter | Y | Testing the second linear pot |
| 02/01/11 | Foam | 70 | 2 | 1 | 3.88 | 1 | 1 | Indenter | Y | Testing the second linear pot |
| 02/28/11 | Foam | 30 | 2 | 1 | 3.88 | 2 | 1 | Indenter | Y | Testing the second spring |
| 04/25/11 | Foam | 30 | 2 | 1 | 3.88 | 2 | 2 | Indenter | Y | Testing the second sled |
| 04/27/11 | Cadavers | 1 | 2 | 1 | 3.88 | 2 | 2 | 1 | Y | Testing the second sled |
| 05/03/11 | Live pigs | 1 | 2 | 1 | 3.88 | 2 | 2 | 1 | Y | Testing the second sled |
| 05/05/11 | Live pigs | 2 | 2 | 1 | 5.82 | 3 | 2 | 1 | Y | Testing the third spring |
| 05/09/11 | Live pigs | 1 | 2 | 1 | 5.82 | 3 | 2 | 1 | Y | Testing the third spring |
| 05/25/11 | Foam | 18 | 2 | 1 | 3.88 | 3 | 2 | Indenter | Y | Testing penetration depth |
| 02/24/12 | Foam | 21 | 2 | 1 | 3.88 | 3 | 2 | Indenter | N | Testing with Qualisys without stopping mech. |
| 02/24/12 | Cadavers | 5 | 2 | 1 | 5.82 | 3 | 2 | 1 | N | Testing with Qualisys without stopping mech. |
| 04/09/12 | Live pigs | 1 | 2 | 1 | 5.82 | 3 | 2 | 1 | N | Testing modifications in vivo |
| 04/23/12 | Live pigs | 2 | 2 | 1 | 5.82 | 4 | 2 | 2 | N | Testing the fourth spring in vivo |
| 04/24/12 | Live pigs | 2 | 2 | 1 | 5.82 | 4 | 2 | 2 | N | Testing the fourth spring in vivo |
| 05/01/12 | Live pigs | 2 | 2 | 1 | 5.82 | 4 | 2 | 2 | N | Testing the fourth spring in vivo |

Note: The associated variables are given, such as linear potentiometer number, rotary potentiometer number, pendulum drop mass, spring number, indenter or mounting mechanism number, and whether or not the stopping mechanism was used. The last column describes the purpose of each impaction test that was performed.
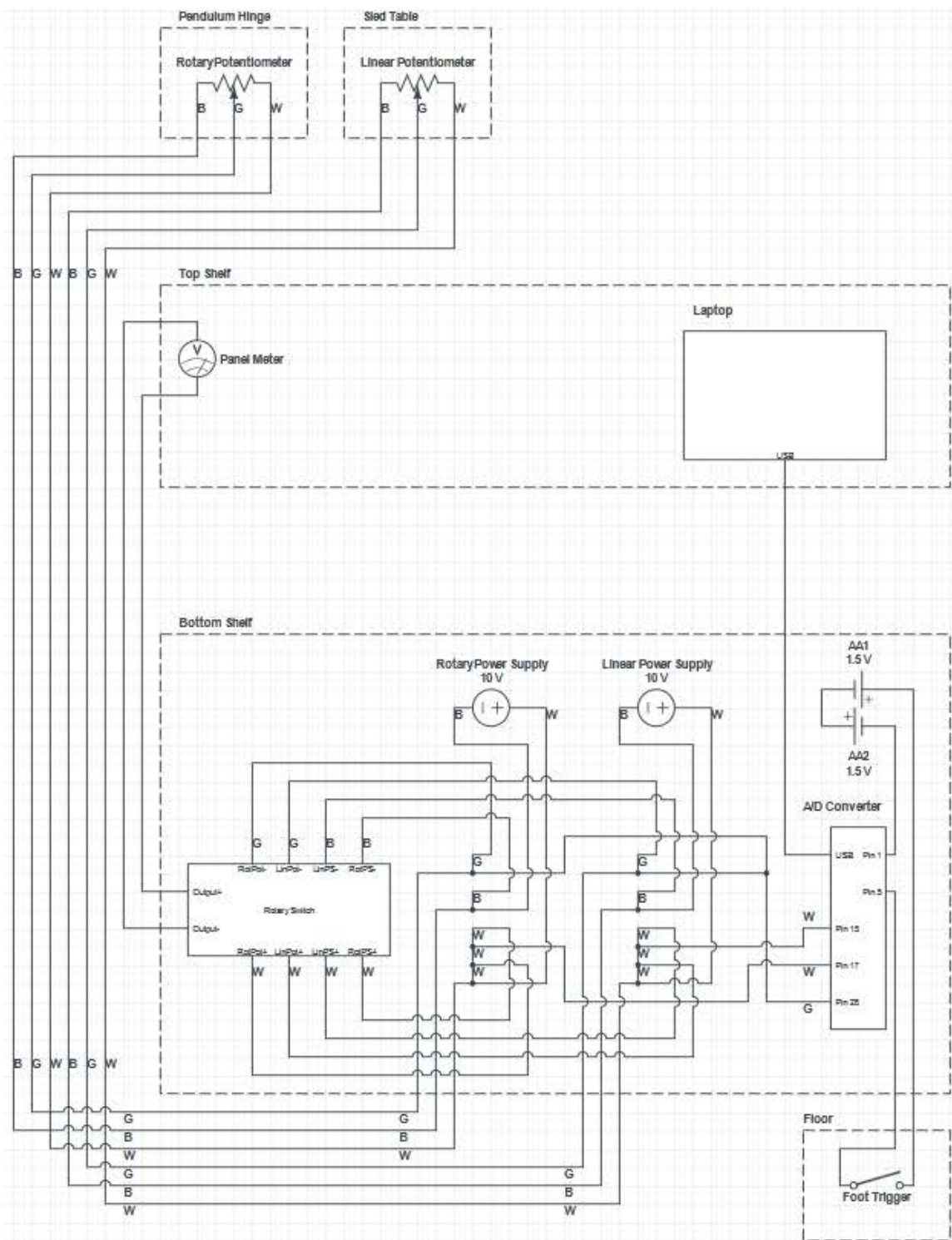
Figure A1: Circuit diagram of the data collection instrumentation and wiring. The letters correspond to the color of wire. The rotary switch has four paired nodes (nodes vertically opposite each other) that correspond to a position that could be cycled through and seen on the panel meter.

REFERENCES

1.      *Osteoarthritis: National clinical guideline for care and management in adults*
        2008: London.

2.      Buckwalter, J.A. and H.J. Mankin, *Articular cartilage: degeneration and
        osteoarthritis, repair, regeneration, and transplantation.* Instr Course Lect, 1998.
        **47**: p. 487-504.

3.      Buckwalter, J.A. and J. Martin, *Degenerative joint disease.* Clin Symp, 1995.
        **47**(2): p. 1-32.

4.      Buckwalter, J.A., J. Martin, and H.J. Mankin, *Synovial joint degeneration and the
        syndrome of osteoarthritis.* Instr Course Lect, 2000. **49**: p. 481-9.

5.      Buckwalter, J.A. and J.A. Martin, *Osteoarthritis.* Adv Drug Deliv Rev, 2006.
        **58**(2): p. 150-67.

6.      Ponseti, I.V., J.A. Maynard, S.L. Weinstein, E.G. Ippolito, and J.G. Pous, *Legg-
        Calve-Perthes disease. Histochemical and ultrastructural observations of the
        epiphyseal cartilage and physis.* J Bone Joint Surg Am, 1983. **65**(6): p. 797-807.

7.      Brown, T.D., R.C. Johnston, C.L. Saltzman, J.L. Marsh, and J.A. Buckwalter,
        *Posttraumatic osteoarthritis: a first estimate of incidence, prevalence, and burden
        of disease.* J Orthop Trauma, 2006. **20**(10): p. 739-44.

8.      Kellgren, J.H., *Osteoarthrosis in patients and populations.* Br Med J, 1961.
        **2**(5243): p. 1-6.

9.      Kirkley, A., T.B. Birmingham, R.B. Litchfield, J.R. Giffin, K.R. Willits, C.J.
        Wong, B.G. Feagan, A. Donner, S.H. Griffin, L.M. D'Ascanio, J.E. Pope, and P.J.
        Fowler, *A randomized trial of arthroscopic surgery for osteoarthritis of the knee.*
        N Engl J Med, 2008. **359**(11): p. 1097-107.

10.     Lee, P., P.J. Rooney, R.D. Sturrock, A.C. Kennedy, and W.C. Dick, *The etiology
        and pathogenesis of osteoarthrosis: a review.* Semin Arthritis Rheum, 1974. **3**(3):
        p. 189-218.

11.     Sharma, L., D. Kapoor, and S. Issa, *Epidemiology of osteoarthritis: an update.*
        Curr Opin Rheumatol, 2006. **18**(2): p. 147-56.

12.     Boden, B.P., F.T. Sheehan, J.S. Torg, and T.E. Hewett, *Noncontact anterior
        cruciate ligament injuries: mechanisms and risk factors.* J Am Acad Orthop Surg,
        2010. **18**(9): p. 520-7.

13.     Roos, H., T. Adalberth, L. Dahlberg, and L.S. Lohmander, *Osteoarthritis of the
        knee after injury to the anterior cruciate ligament or meniscus: the influence of
        time and age.* Osteoarthritis Cartilage, 1995. **3**(4): p. 261-7.

14.     Nikolic, D., Z. Jovanovic, Z. Popovic, R. Vulovic, and M. Mladenovic, *Primary
        surgical treatment of war injuries of major joints of the limbs.* Injury, 1999. **30**(2):
        p. 129-34.

15.    Isaac, D.I., E.G. Meyer, and R.C. Haut, *Chondrocyte damage and contact pressures following impact on the rabbit tibiofemoral joint.* J Biomech Eng, 2008. **130**(4): p. 041018.

16.    Reginster, J.Y., *The prevalence and burden of arthritis.* Rheumatology (Oxford), 2002. **41 Supp 1**: p. 3-6.

17.    Leigh, J.P., W. Seavey, and B. Leistikow, *Estimating the costs of job related arthritis.* J Rheumatol, 2001. **28**(7): p. 1647-54.

18.    Elders, M.J., *The increasing impact of arthritis on public health.* J Rheumatol Suppl, 2000. **60**: p. 6-8.

19.    Gabriel, S.E., C.S. Crowson, and W.M. O'Fallon, *Costs of osteoarthritis: estimates from a geographically defined population.* J Rheumatol Suppl, 1995. **43**: p. 23-5.

20.    Jackson, D.W., T.M. Simon, and H.M. Aberman, *Symptomatic articular cartilage degeneration: the impact in the new millennium.* Clin Orthop Relat Res, 2001(391 Suppl): p. S14-25.

21.    Lapsley, H.M., L.M. March, K.L. Tribe, M.J. Cross, and P.M. Brooks, *Living with osteoarthritis: patient expenditures, health status, and social impact.* Arthritis Rheum, 2001. **45**(3): p. 301-6.

22.    Leardini, G., F. Salaffi, R. Caporali, B. Canesi, L. Rovati, and R. Montanelli, *Direct and indirect costs of osteoarthritis of the knee.* Clin Exp Rheumatol, 2004. **22**(6): p. 699-706.

23.    MacLean, C.H., K. Knight, H. Paulus, R.H. Brook, and P.G. Shekelle, *Costs attributable to osteoarthritis.* J Rheumatol, 1998. **25**(11): p. 2213-8.

24.    Murphy, L.B., C.G. Helmick, M.G. Cisternas, and E.H. Yelin, *Estimating medical costs attributable to osteoarthritis in the US population: comment on the article by Kotlarz et al.* Arthritis Rheum, 2010. **62**(8): p. 2566-7; author reply 2567-8.

25.    Furman, B.D., J. Strand, W.C. Hembree, B.D. Ward, F. Guilak, and S.A. Olson, *Joint degeneration following closed intraarticular fracture in the mouse knee: a model of posttraumatic arthritis.* J Orthop Res, 2007. **25**(5): p. 578-92.

26.    MacKenzie, E.J., M.J. Bosse, J.F. Kellam, A.R. Burgess, L.X. Webb, M.F. Swiontkowski, R.W. Sanders, A.L. Jones, M.P. McAndrew, T.M. Patterson, and M.L. McCarthy, *Characterization of patients with high-energy lower extremity trauma.* J Orthop Trauma, 2000. **14**(7): p. 455-66.

27.    Segui-Gomez, M. and E.J. MacKenzie, *Measuring the public health impact of injuries.* Epidemiol Rev, 2003. **25**: p. 3-19.

28.    McKinley, T.O., J. Borrelli, Jr., D.D. D'Lima, B.D. Furman, and P.V. Giannoudis, *Basic science of intra-articular fractures and posttraumatic osteoarthritis.* J Orthop Trauma, 2010. **24**(9): p. 567-70.

29.     Hembree, W.C., B.D. Ward, B.D. Furman, R.D. Zura, L.A. Nichols, F. Guilak, and S.A. Olson, *Viability and apoptosis of human chondrocytes in osteochondral fragments following joint trauma.* J Bone Joint Surg Br, 2007. **89**(10): p. 1388-95.

30.     Kim, H.T., M.Y. Lo, and R. Pillarisetty, *Chondrocyte apoptosis following intraarticular fracture in humans.* Osteoarthritis Cartilage, 2002. **10**(9): p. 747-9.

31.     Murray, M.M., D. Zurakowski, and M.S. Vrahas, *The death of articular chondrocytes after intra-articular fracture in humans.* J Trauma, 2004. **56**(1): p. 128-31.

32.     Dang, A.C. and H.T. Kim, *Chondrocyte apoptosis after simulated intraarticular fracture: a comparison of histologic detection methods.* Clin Orthop Relat Res, 2009. **467**(7): p. 1877-84.

33.     Muller, F.J., L.A. Setton, D.H. Manicourt, V.C. Mow, D.S. Howell, and J.C. Pita, *Centrifugal and biochemical comparison of proteoglycan aggregates from articular cartilage in experimental joint disuse and joint instability.* J Orthop Res, 1994. **12**(4): p. 498-508.

34.     Setton, L.A., V.C. Mow, F.J. Muller, J.C. Pita, and D.S. Howell, *Mechanical behavior and biochemical composition of canine knee cartilage following periods of joint disuse and disuse with remobilization.* Osteoarthritis Cartilage, 1997. **5**(1): p. 1-16.

35.     Ward, B.D., B.D. Furman, J.L. Huebner, V.B. Kraus, F. Guilak, and S.A. Olson, *Absence of posttraumatic arthritis following intraarticular fracture in the MRL/MpJ mouse.* Arthritis Rheum, 2008. **58**(3): p. 744-53.

36.     Borrelli, J., Jr., M.E. Burns, W.M. Ricci, and M.J. Silva, *A method for delivering variable impact stresses to the articular cartilage of rabbit knees.* J Orthop Trauma, 2002. **16**(3): p. 182-8.

37.     Borrelli, J., Jr., M.J. Silva, M.A. Zaegel, C. Franz, and L.J. Sandell, *Single high-energy impact load causes posttraumatic OA in young rabbits via a decrease in cellular metabolism.* J Orthop Res, 2009. **27**(3): p. 347-52.

38.     Borrelli, J., Jr., K. Tinsley, W.M. Ricci, M. Burns, I.E. Karl, and R. Hotchkiss, *Induction of chondrocyte apoptosis following impact load.* J Orthop Trauma, 2003. **17**(9): p. 635-41.

39.     Borrelli, J., Jr., M.A. Zaegel, M.D. Martinez, and M.J. Silva, *Diminished cartilage creep properties and increased trabecular bone density following a single, sub-fracture impact of the rabbit femoral condyle.* J Orthop Res, 2010. **28**(10): p. 1307-14.

40.     Ewers, B.J., V.M. Jayaraman, R.F. Banglmaier, and R.C. Haut, *Rate of blunt impact loading affects changes in retropatellar cartilage and underlying bone in the rabbit patella.* J Biomech, 2002. **35**(6): p. 747-55.

41.     Milentijevic, D., I.F. Rubel, A.S. Liew, D.L. Helfet, and P.A. Torzilli, *An in vivo rabbit model for cartilage trauma: a preliminary study of the influence of impact stress magnitude on chondrocyte death and matrix damage.* J Orthop Trauma, 2005. **19**(7): p. 466-73.

42.     Rundell, S.A., D.C. Baars, D.M. Phillips, and R.C. Haut, *The limitation of acute necrosis in retro-patellar cartilage after a severe blunt impact to the in vivo rabbit patello-femoral joint.* J Orthop Res, 2005. **23**(6): p. 1363-9.

43.     Szczodry, M., C.H. Coyle, S.J. Kramer, P. Smolinski, and C.R. Chu, *Progressive chondrocyte death after impact injury indicates a need for chondroprotective therapy.* Am J Sports Med, 2009. **37**(12): p. 2318-22.

44.     Yoganandan, N., F.A. Pintar, and R. Seipel, *Experimental production of extra- and intra-articular fractures of the os calcis.* J Biomech, 2000. **33**(6): p. 745-9.

45.     Zhang, H., M.S. Vrahas, R.V. Baratta, and D.M. Rosler, *Damage to rabbit femoral articular cartilage following direct impacts of uniform stresses: an in vitro study.* Clin Biomech (Bristol, Avon), 1999. **14**(8): p. 543-8.

46.     Tochigi, Y., M. Rudert, D. Fredericks, A. Al-Hilli, M. Arunakul, T. Brown, and T. McKinley, *A New Impaction System to Create "Critical" Cartilage Injury in Living Rabbit Knees*, in *OARSI World Congress on Osteoarthritis 2011*September 15-18, 2011, Osteoarthritis Cartilage: San Diego, California, USA. p. S69.

47.     Backus, J.D., B.D. Furman, T. Swimmer, C.L. Kent, A.L. McNulty, L.E. Defrate, F. Guilak, and S.A. Olson, *Cartilage viability and catabolism in the intact porcine knee following transarticular impact loading with and without articular fracture.* J Orthop Res, 2011. **29**(4): p. 501-10.

48.     Callister, W.D.J., *Materials Science and Engineering: An Introduction*1994, New York, New York: John Wiley and Sons, Inc.

49.     Abdel-Wahab, A.A. and V.V. Silberschmidt, *Experimental and numerical analysis of Izod impact test of cortical bone tissue.* The European Physical Journal Special Topics, 2012. **206**: p. 10.

50.     Panagiotopoulos, E., V. Kostopoulos, S. Tsantzalis, A.P. Fortis, and A. Doulalas, *Impact energy absorption by specimens from the upper end of the human femur.* Injury, 2005. **36**(5): p. 613-7.

51.     Zeebroeck, M.V., E. Tijskens, P.V. Liedekerke, V. Deli, J.D. Baerdemaeker, and H. Ramon, *Determination of the dynamical behaviour of biological materials during impact using a pendulum device.* Journal of Sound and Vibration, 2003. **266**: p. 16.

52.     Tochigi, Y., T.E. Baer, P. Zhang, J.A. Martin, and T. Brown, *A New Insult Technique for a Large Animal Survival Model of Human Intra-articular Fracture*, in *OARSI World Congress on Osteoarthritis 2009* September 10-13, 2009, Osteoarthritis Cartilage: Montreal, Quebec, Canada. p. S51.

53.     Tochigi, Y., J.A. Buckwalter, J.A. Martin, S.L. Hillis, P. Zhang, T. Vaseenon, A.D. Lehman, and T.D. Brown, *Distribution and progression of chondrocyte damage in a whole-organ model of human ankle intra-articular fracture.* J Bone Joint Surg Am, 2011. **93**(6): p. 533-9.